LBL--15325

DE83 005450

Intermediate- and High-Energy Reactions
of Uranium with Neon and Carbon

Patrick Lee McGaughey

Ph. D. Thesis

November 1982

Nuclear Sciences Division
Lawrence Berkeley Laboratory
University of California
Berkeley, CA 94720

This work was supported by the Director, Office of Energy Research, Division of Nuclear Physics of the Office of High Energy and Nuclear Physics of the U. S. Department of Energy under Contract DE-AC03-76SF00098.

Intermediate and High Energy Reactions of Uranium with Neon and Carbon

Patrick Lee McGaughey

Lawrence Berkeley Laboratory
University of California
Berkeley, CA 94720

ABSTRACT

Target fragment production from the interactions of 1.0, 3.0, 4.8, and 12 GeV ^{12}C and 5.0, 8.0, 20, and 42 GeV ^{20}Ne with uranium has been measured using off-line gamma-ray spectroscopic techniques. The experimental charge and mass yield distributions are generally consistent with the concepts of limiting fragmentation and factorization at energies of 3.0 GeV and above. The total projectile kinetic energy was found to be the relevant scaling parameter for the comparison of reactions induced by projectiles of different sizes. Light fragments with mass number less than 60 were found to violate limiting fragmentation, and had excitation functions that were strongly increasing with projectile energy until 8.0 to 12.0 GeV. With the 1.0 GeV ^{12}C beam the pattern of mass yields was quite different from that of all the other reactions, with the normal peak in the fission mass region ($80 < A < 145$), but with much lower yields below mass number 60 and between mass numbers 145 and 210, indicating that these fragments are formed primarily in very energetic reactions in which large excitation energies are transferred to and significant amounts of mass are removed from the target nucleus.

Theoretical predictions of the intra-nuclear cascade, nuclear fireball, and nuclear firestreak models are compared with the experimental results. The fireball model is found to be inferior to the other two, due to its failure to deposit large enough excitation energies within the fragment precursors. The intra-nuclear cascade and nuclear firestreak models are both able to predict the general shapes of the experimental distributions, with the exception of the yields for the lightest fragments. However, these two models are found to be incapable of reproducing the typical target fragment recoil velocities, which suggests that some unexpected mechanism must exist for the transfer of large excitation energies to the fragment precursors without the correspondingly large amounts of recoil momenta.

ACKNOWLEDGEMENTS

I would like to take this opportunity to recognize the contributions of a few of those people who have assisted and encouraged me in the pursuit of this thesis work. First of all, let me express my gratitude to Glenn T. Seaborg, my research director, who more than anyone else made this project possible and enjoyable. I also wish to give thanks to my colleagues Walter Loveland, Kjell Aleklett, Diana Lee and David Morrissey for the invaluable assistance which they rendered in performing the experiments, developing the theoretical models, and for their comradery. Finally, special thanks are due to my friends both inside and outside of the scientific disciplines, and to my family, without whom my life at Berkeley would have been much less pleasant.

This work was supported by the Director, Office of Energy Research, Division of Nuclear Physics of the Office of High Energy and Nuclear Physics of the U. S. Department of Energy under Contract DE-AC03-76SF00098.

TABLE OF CONTENTS

I. INTRODUCTION

A. Background

Simultaneous with a series of dramatic advances in accelerator technology that occurred during the 1970's, a new chapter in the study of the properties of nuclear matter was opened. During a period of only a few years, the kinetic energies of the available composite projectiles were increased from a few MeV to a few GeV per nucleon. Projectiles that can presently be accelerated to relativistic energies include ions as heavy as uranium (1). Protons are now routinely accelerated to several hundred GeV. These advances have made possible the study of nuclei undergoing reactions throughout four characteristic energy ranges: the subsonic, supersonic, mesonic, and relativistic domains. These correspond to nuclear collisions in which the center of mass energy is such that the projectile is traveling at a velocity below the speed of sound in nuclear matter, above this speed, above the pion production threshold, and at relativistic velocities, respectively.

Until recently only a fraction of these domains had been explored using accelerators, mainly the subsonic area and the light-mass projectile part of the others. Some experimenters have used cosmic radiation to access the relativistic regime (2), but this method has severe projectile intensity limitations. With the upgrades of the Berkeley Bevalac, the CERN SC synchro-cyclotron, and various cyclotrons, it has become possible to access a much larger part of these energy domains.

Researchers have placed particular emphasis upon the study of relativistic heavy-ion (RHI) induced reactions (3), in which it was expected that nuclear matter might be compressed to abnormally high densities and subjected to extremes of heating (4). Numerous workers have speculated upon the possible formation of nuclear shock waves, density isomers, and pion condensates (5,6). While the existence of these phenomena have had no clear experimental confirmation, there has been substantial recent evidence for the existence of certain anomalies in projectile fragmentation data (7). It has been hypothesized that certain projectile fragments (called anomalons) are formed in a small percentage of RHI-induced reactions and have reaction cross-sections that are much larger than those of normal fragments.

The reactions induced by heavy-ions at high energies have been characterized as belonging to one of two broad classes: peripheral and central collisions (8). This classification can be made according to the impact parameter of the collision. Peripheral collisions occur when the impact parameter is nearly the sum of the radii of the two nuclei. In this case, only the surfaces of the two nuclei are believed to interact, and only a few nucleons are removed from each nucleus during the interaction. The relatively intact fragment precursors separate with only modest excitation energies and momenta imparted by the reaction. Due to the reaction geometry, this process occurs with large probability.

Central collisions occur when the impact parameter is near zero, which has a much lower associated probability. In this scenario the two nuclei overlap nearly completely, and the nature of the reaction is expected to be quite different. Since the nucleon-nucleon mean free paths are quite short in nuclei (9), most of the nucleons in the projectile will suffer multiple collisions while traversing the target nucleus. Thus, the two nuclei are expected to undergo a violent collision with a large amount of the incident energy being converted into internal excitation. The result can be a violent disintegration into a multitude of light fragments and particles.

The observed fragments formed in these two types of reactions have been classified as belonging to one of three categories (8): projectile fragments, traveling at near-beam velocities in a narrow cone around zero degrees in the laboratory frame, target fragments, with near zero velocities, and intermediate products, such as various light fragments and particles, moving at velocities similar to the center of mass of the system. The relative amounts of each of these products that are formed are dependent upon the impact parameter of the collision.

A variety of experimental techniques have been employed for the detection of various of these reaction products (3). The methods employed include the use of emulsion, mica, and plastic track detectors, streamer chambers, recoil spectrometers, particle telescopes, radiochemical techniques, etc.

Due to the previous lack of heavy-mass RHI beams, most of the work concerning heavy fragment production has been carried out by the reaction of heavy targets with light beams. In this work we will concentrate upon the production and detection of heavy target fragments in the target reference frame, remembering that the results are analogous to those observed for projectile fragments observed in the projectile rest frame.

B. Hypotheses of Fragmentation

In the simplest view, relativistic heavy-ion physics may be considered to be a development of high energy particle physics to include multi-baryon systems. Therefore, it was logical that the concepts used in high energy physics be applied to RHI-induced interactions. The hypotheses of "limiting fragmentation" and "factorization" [of cross-sections] (10,11), which were first invoked in the description of single-particle inclusive spectra, may have some value for these more complicated reactions. Due to the complex nature of the projectile, a question of the relevancy of discussing fragmentation in terms of the total incident projectile kinetic energy or of the energy per nucleon (a velocity dependence) naturally arises. A third hypothesis has been introduced (12), which states that the nature of the reaction is determined by the total kinetic energy of the projectile.

1. Limiting Fragmentation

Earlier studies of target fragmentation at relativistic projectile energies have demonstrated that the target fragments formed range in mass from that of the target all the way down to light nuclei such as ^{7}Be (13), with recoil kinetic energies varying from near zero to fission energies (approximately 1 MeV/u) (14). The hypothesis of "limiting fragmentation" states that the distributions of products and their energies, in the respective target or projectile rest frame, approach limiting forms as the bombarding energy increases. This limiting behavior can be qualitatively understood as being due to the fact that as the projectile velocity approaches the speed of light, the projectile-target interaction time approaches a constant value. Thus, it may be expected that the fragment production cross-sections and kinematical properties may become insensitive to further increases in the beam energy.

2. Factorization

The hypothesis of "factorization" of cross-sections is operative in the region where limiting fragmentation is valid, and states that the yield of a particular target (projectile) fragment is independent of the bombarding projectile (target) nucleus, except for a geometric factor due to the size of the bombarding nucleus. For the case of target fragmentation, the yield Y for fragment F from target T and beam B, may be expressed as (15):

$$Y^F_{T,B} = G^F_T \, G_B \qquad [1]$$

where G^F_T depends on the target and the fragment formed, and G_B is dependent only upon the geometry. The effect of factorization is to scale the magnitude of the observed product yields, but not to change the shapes of the distributions. The geometry factor may be expressed as (16):

$$G_B = \pi \, r_o^2 \, (A_T^{1/3} + A_B^{1/3} - d) \qquad [2]$$

where A_T and A_P are the target and projectile mass number, respectively, r_o is the nuclear radius constant, and d is the overlap parameter.

3. Total Kinetic Energy Dependence

In the energy range below that in which the concept of limiting fragmentation is applicable, fragment yields and spectra will vary with the projectile energy. For the comparison of different reactions, it is valuable to know whether the physics of the interaction is dependent upon the total kinetic energy of the projectile or the energy per nucleon (velocity dependent). With the exception of products with mass number near to that of the target and of some fission fragments, most products are formed by reaction of the target with a significant number of nucleons from the projectile. If the interaction proceeds mainly by a collective cascade of nucleons, it might be expected that it is the total kinetic energy of the projectile that is sensed by the target nucleus. This shall be the hypothesis of choice.

C. Previous Studies of Target Fragmentation

A substantial amount of experimental data concerning target fragmentation induced by relativistic heavy-ions and protons has become available in the past few years. Cumming, et al. have studied the reaction of ^{nat}Cu with p, ^{4}He, ^{12}C, ^{14}N, and ^{40}Ar at energies ranging from 0.18 to 28 GeV per nucleon (13,17,18). The onset of limiting fragmentation for the mass yields of all but the lightest fragments was observed at approximately 3 GeV total projectile kinetic energy. The isobaric charge distributions for these products were invariant above 3 GeV, further indicating the validity of this hypothesis. At lower energies the mass yield results scaled with the total projectile kinetic energy, not the velocity. The shapes of the mass yield curves were found to be correlated with the total kinetic energy, providing a sort of temperature measurement.

Factorization of the fragment yields seemed to hold for projectiles with similar total energy and for those with energies in the range of limiting fragmentation. The factorization ratios were found to be consistent with factors based upon simple geometry. The failure of limiting fragmentation for the lightest fragments was attributed to the possibility that these were formed only in the most central collisions, where their formation cross-sections would be enhanced by increasing the projectile size and energy.

Recoil momenta measurements of the target fragments, deduced from thick-target, thick-catcher experiments by use of the two-step vector model, demonstrated that while the inferred excitation energies of the fragment precursors were constant above approximately 3 GeV beam energy, the recoil momenta were varying strongly with projectile energy up to nearly 30 GeV. Also, the size of the projectile seemed important, for at the same total projectile kinetic energy the fragments produced with heavy-ions had larger recoil energies than those formed with protons.

Porile, <u>et al</u>. have studied the fragmentation of ^{nat}Ag by p and ^{12}C (19), and confirmed the validity of the factorization hypothesis for the mass yield and charge distributions, again with the exception of the lightest fragments. The mass distributions for heavy-ion induced reactions were moderately well reproduced using both an abrasion-ablation and an intra-nuclear cascade model calculation. However, the models failed to reproduce the proton-induced reaction results.

Heavy-ion and proton-induced reactions with ^{181}Ta have been studied by many groups. Morrissey, <u>et al</u>. reported that the observed fragment production cross-sections scaled with the total projectile kinetic energy (12). A significant enhancement of light fragment production with heavy-ions, relative to protons, was noted. For the first time it was observed that a fraction of the heavy residues must have been formed in central collisions. A comparison of the mass yield curve with the results of the intra-nuclear cascade and abrasion-ablation model calculations indicated that while both models reproduced the general shapes of the distribution, neither could predict the yields of the lightest fragments.

Recoil properties of these fragments were measured by Loveland, et al. (20). These workers found that while the excitation energies of the fragment precursors were similar for protons and for heavy-ions, the recoil momenta were much larger with heavy-ions. Oertel has confirmed that limiting fragmentation is observed in the mass yield curves and isotopic distributions obtained with a variety of projectiles at energies between 5 and 42 GeV (21), again noting the exception of the light fragments. He also determined factorization to be valid for the ratio of total reaction cross-sections of heavy-ions versus protons.

Kaufman, et al. have examined the interaction of protons and heavy-ions with ^{197}Au (22,23). Their conclusions were similar to those obtained with the Ta targets, with limiting fragmentation being observed for the fragment production cross-sections, but not for the recoil momenta. These authors also confirmed the total energy hypothesis. Aleklett, et al. have measured the cross-sections for the production of gold in the reaction of heavy-ions with ^{209}Bi (24). They reported that the observed relative yields of the gold isotopes showed a similar dependence upon their mass number, regardless of the projectile-energy combination, with the conclusion that the inferred excitation energies of the primary residues remain approximately constant.

A substantial body of data has been published concerning the fragmentation of uranium by relativistic protons. Yu has shown that the charge distributions for target fragments with mass in the fission mass region consist of both neutron deficient and neutron excessive species (25). The neutron excessive fragment mass distribution peaked near mass 110 and was understood to be the result of low-excitation-energy fission of a uranium-like nucleus. The neutron deficient fragment distribution was rather flat and has been attributed to being formed by a deep-spallation process. These conclusions have been confirmed by coincident particle detection measurements made by Wilkins, *et al*. (26) and Warwick, *et al* (27).

Recoil properties and formation cross-sections for these fragments have been reported by Porile, *et al*. (28), Biswas and Porile (29), and Lagarde-Simonoff and Simonoff (30). In general, it was found that the neutron deficient fragment spectra and formation cross-sections vary differently with proton energy than do those of the neutron excessive fragments. The latter have excitation functions that decrease with increasing beam energy and have recoil energy spectra that are independent of the beam energy, while the former have increasing excitation functions and recoil energy distributions that decrease sharply above 3 GeV proton kinetic energy. This reinforces the evidence for the existence of different production mechanisms for these two classes of fragments.

Relative production cross-sections for fragments formed in the interaction of 25 GeV ^{12}C with ^{238}U have been reported by Loveland, *et* al. (31). They observed a large enhancement of the heavy-mass yields, relative to the proton induced reaction, exceeding that expected due to simple factorization. Cole and Porile have investigated the 18.5 Gev ^{12}C induced reaction (32). Here it was noted that the light fragments were enhanced relative to those produced with protons, with the very lightest fragments being most strongly affected.

D. Proposed Study

In this study we will examine the variation of target fragment yields as a function of projectile energy and size for the reaction of intermediate and relativistic-energy heavy-ions with uranium. The method of choice will be gamma-ray radio-analytical measurement of the target fragment production cross-sections. Comparison of these mass yields and charge distributions with those obtained from proton-induced reactions will be used to examine the validity of the three hypotheses of fragmentation. Careful examination of the light fragment yields should provide insight into the underlying reason for their known failure to be subject to limiting fragmentation and factorization. Theoretical calculations of the experimental observables will be performed to help elucidate the mechanisms of fragment formation.

II. EXPERIMENTAL

A. Introduction

Target fragment yields have traditionally been measured using the radio-analytical method, which currently remains in use at several laboratories throughout the world. The method is comprised of the irradiation of an elemental foil with the chosen beam, following which the induced radio-activities are surveyed using a gamma-ray spectrometer. Individual nuclides produced in the interactions are identified by their characteristic gamma-ray decay energies and half-lives. This technique offers the advantage of sensitivity to several orders of magnitude in cross-section and has the benefits of providing for absolute charge and mass determination. Variations of this technique have been employed for the measurement of fragment angular distributions and recoil energy spectra.

Disadvantages of this type of off-line measurement include the inability to measure fragment multiplicities and the necessity for the reaction products to have half-lives of at least a few minutes, so that their decays may be observed. Unfortunately, it is known from fission and high-energy studies that many of the products typically formed in a nuclear reaction have quite short beta-decay half-lives (33). Thus, it was expected that the experimentally observed product yields would be an admixture of directly formed products, and those that summed up part of their isobaric beta-decay chain.

The terms "independent" and "cumulative" yields have been used to categorize products that have been formed directly, with no feeding by radioactive decay of a parent, and those that have been formed by both paths, respectively. As a result of this admixing of different types of yields, it was necessary to correct the group of yields measured from each reaction. This was accomplished by fitting the measured yields to charge dispersion curves using an iterative procedure, with the independent yields serving as a guide. From the calculated isotopic and isobaric yields, the pre-beta-decay mass and charge distributions were constructed.

3. Targetry and Irradiations

The self-supporting targets used in the bombardments consisted of natural or depleted uranium of 25 to 120 mg/cm^2 thickness, surrounded by mylar or aluminum catcher foils, which contained the recoiling fragments. At the beam energies used in this work, there was negligible energy loss in target stacks of these thicknesses (34). In most of the experiments targets of more than one thickness were irradiated. This was to provide for the possibility of extrapolating the fragment production cross-sections to zero target thickness, thereby eliminating any effects due to secondary-particle-induced reactions, which are known to give a significant contribution to the yields at large target thicknesses (13). Depleted uranium was the preferred target, since it has much less background activity. However, the prohibitively high cost of this material prevented its general use.

Table I lists the accelerator, beam ion, energy, flux, and length of irradiation together with the target thickness(es) and catcher material used in each experiment. All of the irradiations, other than with the 1.0 GeV ^{12}C beam, were performed at the Bevalac accelerator facility located at the Lawrence Berkeley Laboratory. This facility consists of the SuperHILAC linear accelerator injecting the Bevatron synchrotron. A schematic diagram of a typical Bevalac target arrangement is shown in Figure 1. The beam exits through a Kapton window at the end of the beam pipe, and then passes through a wire chamber, an ion chamber, the target assemblies, and a final wire chamber. These high-energy beams lost very little energy in any of the objects in the beam path and no vacuum chamber was required.

The wire chambers served the purpose of facilitating the focussing and alignment of the beam throughout the target stack. Generally, the beam focus was approximately one half inch in diameter, and remained unchanged in size and position during the irradiations. An ion collection chamber filled with argon and carbon dioxide (80% Ar, 20% CO_2, 800 mm pressure) was used to measure the beam flux.

The CERN SC synchro-cyclotron accelerator, located near Geneva, was used to provide the 1.0 GeV ^{12}C beam. At this low energy, the irradiations were performed inside a small fast-access vacuum chamber. The beam flux measurement was obtained with the use of an aluminum monitor foil. The flux was calculated from the induced ^{24}Na activity by assuming that the cross-section for the reaction $^{27}Al(^{12}C,X)^{24}Na$ was 24.5 millibarns (35). Because the flux and dE/dX of the beam were so much larger at this energy, it was necessary to use aluminum catcher foils, instead of mylar, to prevent their thermal destruction.

C. Gamma-ray Spectroscopy

1. Measurement Systems

Following the end of each irradiation, the gamma-ray activities induced in the target-catcher foil assemblies were measured with gamma-ray spectrometers for a period of up to six weeks. Each sample assembly was mounted on an aluminum counting card, which was rigidly held in place by a Lucite rack at calibrated distances from the face of the gamma-ray detector. Ten or more sample positions were available to allow for the adjustment of the detector dead time. All measurements were made using Ortec coaxial lithium-drifted and intrinsic-germanium diode detectors.

Each detector was DC coupled to a charge sensitive pre-amplifier, which was connected to a high-rate linear amplifier with matching signal risetime. The amplifier outputs were AC coupled with analog to digital converters (ADCs) using active baseline restoration for good peak resolution at high counting rates. The ADC outputs were in turn connected to pulse height analysis systems, which recorded the gamma-ray spectra on magnetic tape or floppy-disc media. A schematic diagram of a spectrometer system is given in Figure 2. Each system was programmed to collect a 4096 channel spectrum covering the energy rang of about 80 to 2000 keV. Corrections for detector dead times were made by automatically increasing the data acquisition time.

2. Calibrations

Each detectiom system was calibrated for absolute efficiency and energy using standard techniques (36). This was performed using mixed gamma-ray standard sources supplied by the National Bureau of Standards and by Amersham Corporation. Spectra from these sources were recorded at each detector position used during the experiments. To perform the energy calibration, the centroid channel numbers of the gamma-ray peaks were fitted to a cubic equation:

$$E = a_1 + a_2C + a_3C^2 + a_4C^3 \qquad [3]$$

where E is the actual energy of a peak, and C is the centroid channel number. The coefficients (a_i's) were determined using a least squares fit of the known peak energies to the channel numbers. The calibration for each detection system was found to be quite linear, with negligible higher order coefficients.

The detector efficiencies were computed by comparison of the known emission rates of the standard sources with their measured gamma-ray photopeak areas. From the calculated efficiencies, the energy dependence of the detector efficiency was determined using a least squares fit to an equation of the form:

$$F = p_1 [E^{-p_2} - p_3 \exp(-p_4E)] \qquad [4]$$

where F is the detection efficiency for a particular peak, E is the peak energy, and the p_i's are the coefficients. This fitting procedure was performed for each counting position of the detectors. The resulting efficiency fits were found to match the measured efficiencies to within the errors associated with the source intensities and those due to measurement statistics.

An important measure of the quality of a detection system is its experimental resolution. This is especially significant for the spectroscopy of RHI-induced reactions, where hundreds of peaks are observed in a single spectrum, many of which overlap. Therefore, each detection system was set up to provide the best possible resolution by careful adjustment of the amplifier risetime and pre-amplifier compensation, together with the use of active signal baseline restoration and extensive grounding systems. The full-width halfmaximum resolution of each spectrometer was found to be less than or equal to 2.2 keV for the ^{60}Co 1332.5 keV gamma-ray. Using the standard sources, the line-shape for each peak was measured and subsequently fit by least squares methods to a shape consisting of a gaussian function with an exponential tail smoothly joined on each side. This form of line-shape was found fit the peak-shapes of each detector to high accuracy.

D. Data Analysis

1. Peak Analysis

Each gamma-ray spectrum collected during the four to six week period following the end of an irradiation was analyzed using a sequence of computer programs previously developed for this purpose (36). A flowchart for this procedure is given in Figure 3. The first operation was to search out and fit the gamma-ray photopeaks. This was done using a modified version of the SAMPO computer code (37). Using the energy, efficiency, and line-shape calibrations previously determined for each detector, this program de-convoluted each spectrum into individual photopeaks superimposed upon a smoothly varying polynomial background. The accuracy of the fitting procedure was usually good, but the program tended to miss small peaks, and was often unable to resolve superpositions of peaks.

Following the completion of the SAMPO analysis, the resulting tables of gamma-ray activities were sorted by sample name and photopeak energy in preparation for decay curve construction. This was done by searching each sample measurement for the presence of gamma-rays of energy within an interval centered about an earlier observed peak's mean energy. The size of the interval was energy dependent with the form:

$$D = 2 \log_{10} E_m - 3.0 \qquad [5]$$

where D is the width of the energy interval in keV and E_m is the mean gamma-ray energy. In this way, a table of gamma-ray intensities and associated errors, sorted as a function of time, was generated for each sample.

2. Half-life Analysis

In the next step of the data reduction, an interactive decay curve analysis program (TAU2) was used to construct decay curves for the gamma-rays observed in each sample. These decay curves were sequentially presented on a graphics terminal, together with a section of a table of nuclides with gamma-ray energies bracketing the observed energy. The data comprising this abridged table were taken from the work of Binder, et al. (38). From the interactive terminal the investigator was able to choose from a variety of different least square fits to the decay curves, including single or multiple components, growth and decay, and background activities. This flexibility made it possible to fit most decay curves correctly and rapidly. After the fit to each decay curve was completed, the program recorded the nuclidic identifications, half-lives, calculated end-of-bombardment activities, and the associated statistical errors.

3. Cross-section Calculation

Using the activity and nuclidic half-life values determined by this method, the cross-sections for each component of the decay curves were calculated using another computer code. Since large beam fluctuations usually occurred during an irradiation, the form of the usual equation used for the calculation was expanded about a number of short intervals, n, during which there was a relatively constant beam flux:

$$Y = A_0 \,/\, [\, N \sum_{i=1}^{n} \phi_i (\, 1 - \exp(-\lambda t_{bi})\,)\, \exp(-\lambda \sum_{j=i+1}^{n} t_{bj})\,] \qquad [6]$$

where Y is the cross-section, N is the number of target atoms, ϕ_i is the beam flux during the i'th interval, λ is the decay constant, A_0 is the activity at the end-of-bombardment, and the t_{bk}'s are the length of the k'th flux interval. The final output of this computer code was an isotope-ordered list of nuclidic cross-sections, which were computed from the weighted averages of all gamma-rays observed for each particular nuclide in the sample.

It was found to be necessary to review the nuclidic assignments, to ensure that consistent identifications had been made. This screening was done using the following criteria:

(a) The energies of the observed gamma-ray transitions were within 0.5 keV of the literature values.

(b) Each decay curve was resolved into a single unique combination of nuclidic identifications.

(c) The cross-sections calculated for each different transition of a particular nuclide were self-consistent.

(d) All of the gamma-ray lines from a given nuclide with branching ratios larger than the weakest observed transition were found to be present, unless they were masked by another more intense gamma-ray.

This screening procedure eliminated most incorrect identifications; the few that remained were removed in the charge dispersion fitting process to be described later.

An attempt was made to correct the nuclidic cross-sections for the possible effects due to secondary-induced reactions. At relativistic energies, large fluxes of light particles with intermediate energies are created in the more central collisions (39). To permit an investigation of this effect, targets of more than one thickness were irradiated in most of the experiments. By fitting the nuclidic cross-sections to a linear function of target thickness, and extrapolating to zero thickness, the size of the effect could be determined and the appropriate corrections made.

4. Mass and Charge Distribution Calculation

The experimentally measured cross-sections included both independent and cumulative yields; products which were formed directly by particle evaporation and those formed as a result of beta-decay following particle emission. However, the data of interest were the independent nuclidic and isobaric yields. For this reason it was necessary to correct the measurements for the effects resulting from precursor beta-decay. The procedure used was to iteratively fit the experimental nuclidic yields to Gaussian charge distributions (40), functions which represent the distribution of isobaric cross-section among the members of the isobar. For a Gaussian distribution, the independent yield Y(Z,A) can be expressed as a function of the mass yield Y(A) by:

$$Y(Z,A) = Y(A) \left[(2\pi C_z(a)^2)^{-1/2} \exp(-(Z-Z_{mp}(A))^2/2C_z(A)^2) \right] \qquad [7]$$

where $C_z(A)$ is the Gaussian width parameter and $Z_{mp}(A)$ is the centroid atomic number value.

Thus, if three independent yields had been measured for each isobar, it would have been possible to uniquely determine each of the three unknowns in this equation. Unfortunately, this was not possible, since there are no known isobars containing more than two nuclides which are shielded from feeding by beta-decay. In fact, generally very few members of any particular isobaric multiplet were observed in the experiments. The solution to this problem was to assume that the values of the isobaric yield, gaussian width, and centroid position vary slowly and regularly as a function of product mass number. This was expected to be a poor assumption for products with mass number near to that of the target, where the mass yield changes rapidly with mass number. Using this approach, the data from each experiment were grouped by similar mass number, and then a single charge distribution was constructed for each group.

A computer code named MASSY has been written by Otto to perform these calculations (41). From a set of input parameters for $Z_{mp}(A)$ and $C_z(A)$, the code constructed sets of charge distributions for each grouping of the data. Using these distributions, together with the half-lives of the members of each isobaric multiplet, the amount of beta-decay feeding to each observed nuclide was computed. Then, the independent yields were calculated, and their distributions were compared to those generated by the original choices for the widths and centers of the charge distributions. A set of parameters that gave reasonable fits to the calculated independent yields were found by iteration. From the independent yields, the mass (isobaric) yields were calculated using equation 7.

III. THEORETICAL MODELS

A. Introduction

At relativistic energies heavy-ions may undergo two basic types of interactions, which can be classified as peripheral and central collisions. Peripheral events are reactions in which there is only a small overlap of nuclear density. Thus, only a small transfer of momentum and energy occurs. The projectile fragments continue forward within a narrow fragmentation cone (in the laboratory frame) at velocities close to that of the incident beam. The slowly recoiling target fragments evaporate particles isotropically and may fission if sufficiently heavy. Central collision events correspond to those reactions in which a nearly complete overlap of the two nuclei takes place. In these events fragmentation products are emitted with large velocities over all forward angles and are no longer of traceable parentage. The high charge multiplicities of these fast fragments indicate that an "explosion" of the colliding system may have occurred. Of course, these scenarios represent the two extreme cases of reactions, and in reality it is expected that all manner of collisions with intermediate character will take place.

To aid in the understanding of the mechanism(s) involved in these two types of interactions, it is important to compare the predictions of current theoretical models with the results of the experimental measurements. Three theoretical models of high-energy heavy-ion-induced reactions will be considered: the intra-nuclear cascade model (42), the nuclear fireball (abrasion-ablation model) (43), and the nuclear firestreak model (44). These three represent somewhat limiting views of relativistic nuclear collisions, with the intra-nuclear cascade model picturing the interaction as consisting of uncorrelated collisions between individual nucleons from the two nuclei, while the nuclear fireball and firestreak models assume that the interaction is localized to collective inelastic collisions of the nucleons within the overlap region, with little effect on the non-overlapping regions of the two nuclei.

Each of these models is based upon the common underlying assumption that the nuclear reaction occurs as a two step process, as originally proposed by Serber (42). During the first step, the fast projectile-target interaction occurs, in which the excited primary projectile and target remnants are formed. The second step consists of a slow statistical de-excitation of these remnants by particle emission and by fission.

There have been alternate theoretical approaches suggested to model these high energy reactions. Campi and Hufner have had some success in fitting experimental data by treating the first step of the reaction with Glauber theory and the second by solution of the Master equation (45). Their results are quite similar to those predicted by the use of the intra-nuclear cascade model. Most recently, fragmentation processes have been approximated using a relativistic hydrodynamic model (46), which views the reaction as being completely collective in nature. However, this work has not yet been applied to quantitatively predict the formation of large target fragments.

B. Intra-nuclear Cascade Model

The first realistic calculations of the interaction of high energy particles with complex nuclei were done within the framework of the intra-nuclear cascade (INC) model (42), which approximates the nuclear reaction as consisting of a sequence of single nucleon-nucleon collisions taking place between the incident particles and the nucleons in the target nucleus. Struck nucleons in the target are similarly allowed to interact with the remaining undisturbed nucleons, until the time at which all the "participant" nucleons have either escaped from the target remnant or have been slowed to energies below the Fermi energy in the target. This type of calculation is particularly well suited to computation using Monte-Carlo simulation techniques on a mainframe computer.

As a representative example of this type of calculation, the Yariv and Fraenkel version of the INC model, named ISABEL (47), was chosen for this work. This computer code has been well described previously; here only the main assumptions used in the calculation will be noted:

(a) The target and projectile nuclei were assumed to behave as cold Fermi gases contained in potential wells. Their nuclear density distributions were approximated by a step function consisting of eight constant density regions. These regions were obtained by fits to folded Yukawa sharp-cutoff density distributions.

(b) The reaction kinematics were treated within the framework of relativistic classical mechanics, with all calculations being performed in the target rest frame, where the projectile was Lorentz contracted.

(c) Within the computation, the multiple collision process was handled in stepwise time fashion. Interactions between cascade particles were not allowed; hence nucleon-nucleon correlations were disregarded.

(d) Pion production and absorption was included and occurred via the delta (3,3) resonance :

$$N + N = \Delta_{3,3} + N \quad [8]$$

$$\Delta_{3,3} = \pi + N \quad [9]$$

where N is a nucleon, and π is a pion.

Nucleon-nucleon and pion-nucleon scattering cross-sections were interpreted from on-mass-shell, free-particle data.

(e) Effects of the Pauli principle were included.

(f) During the development of the cascade process, the densities of the nuclear Fermi seas were depleted, and no further interactions were allowed in the holes created. Each cascade particle was followed until it left the nucleus or until its energy fell below the cutoff for escaping.

Typically, 500 or more complete cascades were performed, with randomly chosen impact parameters. A complete record of the residual mass, charge, excitation energy, recoil momentum, and angular momentum of the projectile and target remnants was kept for each collision. After the computation of the fast cascade process was completed, the target remnants formed in the primary interaction were de-excited using the Monte-Carlo statistical evaporation code described at the end of this chapter.

C. Nuclear Fireball Model

The nuclear fireball model, as originally proposed by Westfall, et al. (43), was developed to account for intermediate velocity nucleon emission resulting from central and near central collisions. It was based upon the geometrical concepts of the abrasion-ablation model of Bowman, et al. (48) and included the use of a relativistic statistical thermodynamic treatment of the participant nucleons. The model may be stated as follows: When the target and projectile collide, the two nuclei make a clean cut through each other. The interaction is localized to the region of overlap, with the non-overlapping regions (spectators) being unaffected. Nucleons in the region of overlap transfer their momenta and energies to the center of mass of the "fireball" that they form, which travels forward at an intermediate velocity.

This "fireball" contains internal excitation energies which are far in excess of normal nuclear binding energies, and is assumed to decay as a non-rotating thermally equilibrated relativistic ideal gas. After undergoing an isotropic expansion in its rest frame, the resulting fast particles have a Maxwellian kinetic energy distribution. In contrast to this, the target and projectile remnants are assumed to have rather low excitation energies and will decay by statistical particle emission and by fission.

A computer code written by Morrissey, et al. named WOOPS (49), was used to perform the fireball model calculations of target fragmentation. In this computation the target and projectile were assumed to be sharp spheres with uniform density distributions, and made a cylindrical cut through each other during the primary interaction. The number of nucleons removed from the target nucleus at each impact parameter was calculated by numerical integration of the intersection volume. By having weighted each impact parameter by its geometrical probability, the cross-sections for each fragment mass were evaluated. The average ratio of the number of removed neutrons to protons was assumed to be equal to the ratio present in the original target nucleus.

Excitation energies for each target remnant produced in the primary encounter were assigned by assuming that the only form of excitation energy present was that due to nuclear deformation of the remnant. This has been referred to as the "clean cut" approximation. The excitation energy was taken to be the product of the nuclear surface energy coefficient (.95 MeV/fm^2) and the increase in nuclear surface area of the deformed fragment relative to that of a spherical nucleus of identical volume. This was also computed by numerical integration. As a result of the "clean cut" approximation, the linear and angular momentum transferred to the fragments were assumed to be negligible and the results of the reaction are independent of the projectile energy. Oliveira, _et al_. have previously shown that this method of calculating the excitation energies of the fragments gives values which are too low to account for the experimental results (50).

To generate the charge distributions for the primary target remnants, it was necessary to consider realistic neutron-proton fluctuations. Morrissey, _et al_. have proposed that these fluctuations could be related to zero point vibrations of the giant dipole resonance (GDR) of the target nucleus (49). This resonance has been postulated to be a collective vibration of neutrons against protons in a nucleus. Using Myers, et al. treatment of the GDR in terms of the nuclear droplet model (51), these workers were able to treat the fluctuations by expressing them in terms of a Gaussian distribution with width based upon the classical turning point of a simple harmonic oscillator. This approach was found to give better fits to experimental fragmentation data than by the assumption that there existed a purely statistical distribution of protons and neutrons throughout the target nucleus before the interaction took place.

Once the calculation for the formation of the primary remnants was complete, these remnants were de-excited using the same model used with the intra-nuclear cascade model calculation.

D. Nuclear Firestreak Model

The rather simple nuclear fireball model suffers from some serious limitations when used for target fragmentation calculations. Specifically, it is expected that the actual amount of excitation energy deposited during the abrasion step must be much larger than that which nuclear deformation alone can supply. In addition, the simple "clean cut" geometry is an over-simplification, since there is significant momentum transfer to most target fragments and there exists some projectile energy dependence of the fragment yields.

In order to retain the collective nature of the nuclear interaction, but to eliminate the unrealistic assumptions of the nuclear fireball model, we have extended the nuclear firestreak model of Myers (44) to include a calculation of the primary projectile and target remnant production in these reactions. Gosset, et al. have previously employed the nuclear firestreak model for the calculation of the spectra of pions, protons, and light nuclei produced in RHI-induce collisions (52).

Under this newer model's formalism, the colliding nuclei are assumed to have diffuse surfaces, which were generated by folding a short-range (Yukawa) function into the conventional sharp-sphere density distribution. It was assumed that during the collision the interaction was localized to the overlap region, where collinear tubes of nuclear matter from the target and projectile underwent completely inelastic collisions. A transparency function, based upon a fixed nucleon-nucleon scattering cross-section of 30 millibarns, was included to prevent collisions from occurring between tubes containing an insufficient density of nucleons.

Once two tubes had collided, they fused and equilibrated their kinetic and thermal energies. If the resulting kinetic energy of a fused tube was less than its binding energy in the target remnant, then it was retained and contributed directly to the remnant's energy, mass, and momenta, which were explicitly conserved during the interaction. Additional excitation energy, due to the surface deformation of the remnant, was included. Charge distributions for the primary remnants were computed using the GDR model mentioned previously. Projectile fragmentation can be calculated in analogous fashion with this code, by reversing the assignments of the projectile and target nuclei. The de-excitation step of the reaction was handled in identical fashion to those of the previously described reaction models and is described in the following section.

E. Statistical De-excitation Model

Each of the previously described reaction models required the use of a statistical de-excitation calculation for the second step of the reaction. In this step the excited primary fragments were assumed to decay by particle emission and by fission into the nuclides (and their beta-decay precursors) that were actually observed in the experiments. So as not to obscure any differences in the results of the three primary reaction models, the identical de-excitation calculation was performed for each.

We have adapted the DFF computer code of Dostrovsky, _et_ _al_. (53) for this calculation. The DFF code is the original stepwise Monte-Carlo treatment of the de-excitation of nuclei by particle emission and fission. The computation was performed according to the following points:

(a) De-excitation was simulated by statistical evaporation of neutrons, protons, deuterons, tritons, ^{3}He, and alpha particles in competition with fission.

(b) Fermi-gas level densities with pairing correction and level density parameter of $a = A/20$ were used.

(c) Effects due to angular momentum were excluded.

In order to obtain a more realistic treatment of fission competition, we have replaced the fission section of the code. In this new section, the excitation energy dependence of the ratio of fission to particle emission widths is given by (54):

$$\Gamma_f / \Gamma_n = \frac{4A^{2/3} a_f (E^*-B_n) \exp[2a_n^{1/2}(E^*-B_n) - 2a_f^{1/2}(E^*-E_f)^{1/2}]}{K_o a_n [2a_f^{1/2}(E^*-E_f)^{1/2}-1]} \qquad [10]$$

where Γ_f and Γ_n are the fission and neutron emission widths, respectively, A is the mass number of the nucleus, E^* is the excitation energy, B_n is the neutron binding energy, E_f is the fission barrier height, and K_o is the projection of the neutron angular momentum upon the nuclear symmetry axis.

The ratio of the level density parameter at the fission saddle point, a_f, to that at the equilibrium deformation, a_n, was arbitrarily set using the relation:

$$a_f/a_n = [\ 1 + 0.1/\log_{10}(E^*-E_f)\ ] \qquad [11]$$

The fission barrier heights were chosen using the approximate formulae from Cohen and Swiatecki (55):

$$E_f = 0.38\ (0.75 - X)\ E_s^o \qquad \text{for } 1/3 \leq X \leq 2/3 \qquad [12]$$

$$E_f = 0.83\ (1.0 - X)^3\ E_s^o \qquad \text{for } 2/3 \leq X \leq 1 \qquad [13]$$

for which the fissionability parameter, X, is given by:

$$X = Z^2 / [\ 50.88\ A\ (\ 1- 1.7826[(A-2Z)/A]^2\ )\ ] \qquad [14]$$

and with

$$E_s^o = 17.80\ A^{2/3} \qquad [15]$$

The variation of the width of the fission mass distribution as a function of the mass, charge , and excitation energy of the fissioning system was determined using the liquid drop theoretical method of Nix (56).

Several thousand de-excitation chains were followed for each model calculation. The averaged results of these simulations are the theoretical analogs of the experimental mass and charge distributions, which are all compared in the next section.

IV. RESULTS AND DISCUSSION

A. Experimental Results

1. Effects Due to Secondary-induced Reactions

In each experiment in which more than one thickness of target was irradiated, the dependence of the fragment production cross-sections upon target thickness was examined. In general it was found that no consistent, statistically significant effect was observed for individual nuclides produced in any particular reaction. To enhance the statistics obtained from the fitting of the observed yields to the target thicknesses, the nuclides observed in each experiment were separated into five groups consisting of fragments that were expected to be produced by similar types of reactions: light fragments with mass number $A < 80$, neutron deficient fragments with $80 < A < 145$, neutron excessive fragments in the same mass range, heavy fragments with $145 \leq A \leq 210$, and near-target fragments with $A \geq 230$.

Within each group, the results from the fitting procedure were averaged to give an approximate correction factor for secondary induced reactions in each group of yields. Even with this rather extreme measure, the statistical errors in the calculated secondary effects were still usually larger than their values, or the calculated effects were smaller than the uncertainties present in the original data. The only group in which there was any hint of a secondary effect being present was the one consisting of neutron excessive fission fragments. Therefore, it was assumed that there was no significant dependence of the target fragment production cross-sections upon the target thicknesses in any of the experiments performed. The results for the directly measured yields were simply averaged over the various different target thicknesses.

2. Charge Distributions

For the purpose of obtaining the independent and isobaric yields, the averaged nuclidic yields were placed into one of sixteen groups according to the mass number of the nuclide and its position with respect to the line of nuclear stability. Each member of a particular group was fitted to a Gaussian-shaped independent yield distribution, as described previously. The nuclidic groupings, together with the centers and widths of the Gaussian distributions, are given in Table II. With the exception of the 1.0 GeV ^{12}C induced reaction, the parameters for each group's fitted distributions are nearly the same in each experiment, indicating that identical fragments were initially formed in each of these reactions with generally similar excitation energies.

The most probable atomic number values (Z_{mp}) used for the centers of the charge distributions are consistent with those determined by Yu for the 11-29 GeV proton-induced reaction (25), the two sets being within less than 1.5 Z units of each other for all of the mass regions. The Z_{mp} values obtained from the 1.0 GeV ^{12}C induced reaction are within 1.5 Z units of those reported by de Saint Simon, _et al._ (57), who have measured the mass distributions of Rb and Cs from the reaction of 77 A MeV ^{12}C with ^{238}U.

Representative charge distributions from the reaction of 3.0 GeV ^{12}C with ^{238}U are shown in Figures 4 through 19. The distributions measured in each of the other reactions are quite similar, with the main differences being only those due to overall changes in the isobaric yields. In the fission mass region ($80 < A < 145$), the charge distributions were found to be composed of two separate distributions, one neutron excessive and the other neutron deficient. These distributions have a separation of from less than two units of atomic number at mass number 90 to approximately four units at mass number 135. This behavior has also been noted in the work of Yu (25) and de Saint Simon _et al_. (57). Warwick, _et al_. (27) have suggested that these two distinct distributions are formed as a consequence of this mass region being populated by two separate reaction mechanisms, one being deep-spallation and the other medium-energy fission.

3. Mass Distributions

Presented in Figures 20 through 27 and in Table III are the yields for each isobar produced in the various reactions, obtained by integration of the charge distributions. Outside of the fission mass range, these are the isobaric yields. Inside this range, they are the isobaric yields of the neutron deficient and neutron excessive distributions. The solid curves shown in the figures represent an approximate fit to the total isobaric yields. The error bars on the measured points reflect only the measurement statistics and do not take into account any errors due to uncertainties in the absolute beam flux or those introduced in the charge distribution curve fitting process. Morrissey, _et al_. (12) have suggested that individual yields may have systematic uncertainties of approximately 25 percent. The observed scatter in the yields indicates that this may be an underestimate. Since it is expected that the mass yield changes slowly over a narrow range of mass (except near the target mass), it is believed that this scatter is not significant, and the averaged values may be used as the isobaric yields.

All of the experimental mass yield curves have some features in common. Most of the isobaric yield lies in the neutron excessive fragments found in the fission mass region, which are formed as the result of fission of a uranium-like nucleus. These fragments are identical to those that are formed in low-energy proton or alpha-particle-induced fission of uranium. A large part of the remaining isobaric yield is also contained in this mass region, and consists of neutron deficient yields. These may have been produced both in high-excitation-energy fission events and by deep-spallation processes. This possibility is indicated by the fact these yields are generally larger than those for the fragments with larger mass, which are expected to be purely spallation yields. In all of the reactions studied a strong increase in the mass yields is observed for the near-target products, as expected, since these are most likely formed in peripheral reactions, which should have large cross-sections.

The energy dependence of the fragmentation of uranium by heavy-ions is demonstrated in Figure 28, in which the isobaric yield curves for the four energies of ^{12}C are superimposed, and likewise in Figure 29 for the four energies of ^{20}Ne. In the case of the 1.0 GeV ^{12}C projectile there is a large peak in the fission mass region, with rather low yields everywhere else except near to the target mass. The neutron deficient yields in the fission mass region are much larger than the spallation yields at larger mass, indicating that most of the former are produced by the fission of a highly excited system.

As the ^{12}C bombarding energy increases, two dramatic changes in the yield patterns are apparent. Of greater significance, a large increase in the production of the light fragments (A < 60) is observed, with the very lightest fragments showing the largest effect. This increase continues up to the highest energy of 12 GeV, suggesting that the mechanism for the formation of these fragments is quite energy intensive. Gutbrod, et al. (58) have suggested that the formation of the lightest fragments can be accounted for by assuming that they are emitted from a highly excited thermal source. If this is the case, then the probabilities for their formation are related to their size and to the temperature of the sources, which are directly dependent upon the beam energy. The shapes of the light fragment yield distributions measured in this work seem to be exponential up to about mass number 50, as would be expected if they were produced thermally.

A large change is also observed in the yields of the heavy fragments ($145 \leq A \leq 210$). These increase sharply as the projectile energy increases from 1.0 to 3.0 GeV and then seem to become relatively constant at higher energies. The bump observed at mass number 175 in the yield curve from the experiment performed at 12 GeV may not be significant, since there are few experimental points in this region. No evidence is seen for a very large peak in the yields of mass number 160 to 180 fragments, as originally reported by Loveland, et al. for the reaction of 25.2 GeV ^{12}C with ^{238}U (31). A re-analysis of that work has determined that the fitting of the independent yields to the charge distributions may have been performed incorrectly, resulting in abnormally large yields (59). The yields of fragments in the fission mass region seem to be nearly independent of the projectile energy. While there appears to be some increase in these yields going up in energy from 1.0 to 3.0 GeV, this could simply be due to the choice of the monitor cross-section that was used to calculate the beam flux for the 1.0 GeV experiment being somewhat too large.

Much less variation of the yields with projectile energy is observed with ^{20}Ne , as expected, since its lowest total kinetic energy was 5.0 GeV. With this projectile the mass yield curves are all quite similar, except for a problem with the overall height of the yields obtained from the reaction induced at 5.0 GeV. Apparently, in this experiment there was an undiagnosed difficulty with the ion chamber and the associated electronics that were used to measure the beam flux, with the result being that an erroneously small flux was recorded. This problem is clearly demonstrated in the table of total reaction cross-sections to be introduced in the following section. If the height of this yield curve is normalized to that of the others, an increase in light fragment production is observed as the energy increases from 5.0 to 8.0 GeV. At higher energies little further change is apparent. The heavy element yields are all similar, with the increase at 20 GeV again probably being due to the scarcity of data in this region. Yields of the fission mass products are relatively constant at all these energies.

With the confirmation of limiting fragmentation for all but the lightest fragment's yields at approximately 3.0 GeV, it is of interest to make some tests for factorization. In Figure 30 the isobaric yields for the 4.8 GeV ^{12}C and 5.0 GeV ^{20}Ne-induced reactions are compared. Again with some variation in the heavy mass region, the yield patterns are nearly identical. The good agreement for even the lightest fragments confirms the viability of both the factorization and the total energy hypotheses.

Heavy-ion and proton-induced reactions are compared in Figure 31. The two isobaric yield curves are for the reactions of 29 GeV protons and 20 GeV ^{20}Ne with ^{238}U. The proton data were taken from the work of Chu, et al. (60). The variation of isobaric yield with product mass number is similar for both reactions, except for the flatness at the top of the fission bump from the proton-induced reaction. Yu has re-analyzed these proton data (25) and concluded that there should be a peak in this region, which would be in better agreement with the heavy-ion data. Heavy fragment yields, which were not reported in the original proton work, have since been measured by Jacak, et al. (61). These workers observed cross-sections of about 5 to 10 millibarns for fragments of mass numbers 150 to 200, which are in agreement with those seen in this work, keeping in mind the difference in total reaction cross-sections.

4. Total Reaction Cross-sections

In order to further check the various hypotheses of fragmentation, it is useful to examine the total reaction and total fission cross-sections. These were determined by integrating the mass yield curves according to the following points:

(a) The lower limit of the integration was set at mass number 40. The origin of fragments with lower mass is uncertain and thus their multiplicities are unknown. In some cases these fragments may have even been formed in conjunction with a heavy fragment.

(b) All of the fragments from within the fission mass region ($80 < A < 145$) were assumed to have been produced by binary fission.

Therefore, their yields were divided by two before integration. While some of the neutron deficient products in this group may have been produced by spallation, most were probably of binary origin.

(c) The upper limit of the integration was mass number 230. This choice helped to eliminate fragments that were formed in the most peripheral reactions, such as coulomb excitation, from making large and uncertain contributions to the total reaction cross-sections.

The total reaction and fission cross-sections obtained in this manner are presented in Table IV. The experimental values are expected to have errors of approximately 25 percent. These data show that the total reaction cross-section for a RHI-induced reaction of uranium is generally invariant as the total projectile kinetic energy is varied from 3.0 to 42 GeV. The deviations observed for the 1.0 GeV ^{12}C and 5.0 GeV ^{20}Ne-induced reactions have been previously discussed. Excluding these two measurements, the values of the total reaction cross-sections for ^{12}C and ^{20}Ne with ^{238}U agree rather well with the respective geometric values of 3.75 and 4.16 barns. The latter values were calculated using Equation 2, taking the parameters r_0 and d to be 1.37 and 5.1 fm, respectively, as suggested in the work of Heckman, _et al_. (62). The average experimental cross-section ratio for ^{20}Ne relative to ^{12}C is 1.22, which is well within the error of the ratio of 1.11 for the geometric cross-sections. No evidence is seen in the experimental total reaction cross-sections for any effects due to nuclear transparency. Since the free nucleon-nucleon scattering cross-sections vary dramatically with kinetic energy (63), there existed the possibility that the total reaction cross-sections would be energy dependent, but this appears not to be the case.

The fraction of total reaction cross-section going into the fission channel seems to be relatively constant at all but the lowest energy, with an average value of about .56 at energies above 1.0 GeV. This is nearly identical to the value of .58, which was calculated in a similar manner from the results presented by Yu for 11-29 GeV protons (25). Track detector measurements of total fission cross-sections from the reaction of various energies of ^{14}N with uranium have been made by Katcoff and Hudis (64), and match nicely those obtained from the ^{12}C-induced reaction.

B. Theoretical Model Predictions

1. Theoretical Mass and Charge Distributions

In Figures 32 through 39 the mass yield distributions predicted by the intra-nuclear cascade (INC), nuclear firestreak, and nuclear fireball models are presented, together with the experimental results previously described. Since the nuclear fireball model includes no projectile energy dependence, its results are shown only once for each choice of projectile. From an examination of Figures 35 and 38, it is evident that this model drastically overestimates the yields of the heavy fragments and underestimates those of the fission mass fragments. This is primarily due to the very low excitation energies which are deposited during the first step of the model reaction, which are in turn the consequence of the "clean cut" assumption. As earlier noted, Oliveira, et al. have come to this same conclusion (50). Of course, by altering the a_f/a_n ratio used in the de-excitation calculation, it would be possible to allow more fission to occur. However, even for larger values of this ratio, too few of the heavy residues will fission before losing their excitation energy by particle emission.

In contrast to the predictions of the nuclear fireball model, both the nuclear firestreak and INC models reproduce the experimental yield curves with fair accuracy. For the 1.0 GeV ^{12}C experiment these two calculations follow the shape and approximate size of the fission mass distribution but underestimate the heavy fragment yields for mass numbers 175 to 210. Of course, it should be kept in mind that the theoretical yields in this region are quite sensitive to the choice of the a_f/a_n ratio. As the projectile energy increases to 3.0 GeV, the calculations begin to fill in the yields of the heavy fragments, so that they approach the experimental values. Further increases in projectile energy have little effect upon the theoretical yields of these fragments, but do result in yields that become too large for fragments of mass numbers 50 to 80. Neither model is capable of predicting the turn-up in the yields for fragments with mass numbers less than 50, which is apparent in the experimental data. This failure can be attributed to the possibility that these fragments are not formed in binary fission, which is their assumed mechanism of formation in the model calculations.

Two primary differences between the nuclear firestreak and INC model results can be noted. The nuclear firestreak calculation generally predicts somewhat larger yields for the mass numbers at and below the lower end of the fission region. This is due to the larger excitation energies that are deposited during the first step of the reaction, which result in larger numbers of particles being emitted in the de-excitation step. The other difference between the model calculations is the apparent lack of large near-target yields that is predicted by the firestreak model at most projectile energies. This is simply an artifact of the interpolation process that was used in the calculation to predict the average excitation energy for each primary fragment mass that was formed during the primary reaction. A correction could be made for this by the use of a discrete distribution of excitation energies for the near-target primary fragments.

It is of some interest to examine the charge distributions that are predicted by the various models. However, the widths and centers of these distributions turn out to be much more dependent upon the parameters used in the de-excitation model, than upon the choice of fragmentation model, except possibly for products with mass near to that of the target. This has been noted previously by Morrissey, et al. (65). Hence, a comparison of the predicted charge distributions with those determined in the experiments can serve best as a test of the accuracy of the de-excitation model. In Figure 40 the predicted charge distribution for products with mass numbers 40 to 60, which was calculated through use of the intra-nuclear cascade model, is compared with the experimental independent yields for the reaction of 3.0 GeV ^{12}C with ^{238}U. The center and width of the theoretical distribution are similar to those of the experimental data, with the former being centered somewhat more neutron excessive. Throughout the non-fission mass regions the theoretical centers of the distributions are generally within less than 1.5 Z units of those obtained from the experiments. For fission mass products the calculations give single broad charge distributions, which superimpose over the tops of the twin narrow distributions of neutron excessive and deficient fragments which are observed in the experiments.

It is somewhat surprising that two models as conceptually dissimilar as the intra-nuclear cascade and nuclear firestreak models should give such similar results. This can be interpreted as being due to the following factors: First, many of the features of RHI-induced reactions are simply dependent upon the geometry of the collision, which is treated nearly identically in both models. Second, the mean free path of a cascade nucleon in a nucleus is short enough at these energies so that its interaction is quite inelastic, giving results which approach those obtained as a consequence of the assumption of a completely inelastic interaction, which is inherent in the nuclear firestreak model. Finally, it is the de-excitation process which takes place in the common second step of the reaction that generates the general shape of the mass yield distribution. As long as the excitation energies deposited in the first step are comparable, the resulting shapes of the yield distributions will be quite similar.

While the intra-nuclear cascade and nuclear firestreak model results reproduce much of the character of the experimental data for these reactions, neither model accurately satisfies the hypothesis of limiting fragmentation. This is a consequence of the fact that both models predict that the excitation energies of the fragment precursors continue to increase throughout this projectile energy range. Yet these models do demonstrate the validity of the concepts of factorization and a dependence upon the total kinetic energy for the results of the reactions.

2. Theoretical Recoil Velocity Distributions

As a parallel to this study, we have previously reported the target fragment energies and momenta measured in the reactions of 4.8 GeV ^{12}C and 5.0 GeV ^{20}Ne with uranium (66). A comparison of the recoil velocities for neutron deficient fragments produced in the 4.8 GeV ^{12}C-induced reaction with the velocities predicted by the nuclear firestreak and INC models is shown in Figure 41. The selection of neutron deficient fragments was made to eliminate the products of low-excitation-energy fission and to emphasize fragments produced in deep-spallation type reactions. The lines of recoil velocity shown for the model calculations were determined by allowing the target remnants produced in the first step of the reaction to de-excite by particle emission only. A cursory examination of this figure reveals a rather dramatic failure of the models; except for the near-target fragments, both models grossly overestimate the recoil velocities that are imparted to the fragments. This failure is especially significant at mass numbers above 150, since these fragments are expected to be formed only by a deep-spallation type of mechanism.

It is difficult to understand the behavior of the experimental recoil velocity distributions in terms of conventional theory. The recoil velocities are nearly identical for all fragments of mass numbers 100 through 200. This is hard to reconcile with the supposition that these fragments are formed by de-excitation of primary remnants that were given widely different amounts of excitation energy during the fast abrasion step of the reaction. Apparently, some mechanism exists which allows for the transfer of large amounts of excitation energy to the fragments, without the transfer of correspondingly large amounts of linear momentum. Crespo, *et al.* have proposed that the primary remnants could have emitted large pre-equilibrium fragments such as Na (67), which carried off large amounts of momenta before the statistical de-excitation took place. This mechanism could therefore account for the large recoil velocities of these light fragments, as well as their strongly energy dependent excitation functions.

3. Theoretical Total Reaction Cross-sections

The total reaction cross-sections predicted by the intra-nuclear cascade and nuclear firestreak models are given together with the experimental values in Table IV. Both calculations predict a general invariance of reaction cross-section with beam energy. They match the experimental values reasonably well, except for the measurements with the 1.0 GeV ^{12}C and 5.0 GeV ^{20}Ne beams, which are somewhat suspect, as discussed earlier. This general agreement is simply the result of the geometrical assumptions inherent in the two models.

V. CONCLUSIONS

Several conclusions can be drawn from the results presented in the previous section. Clear evidence for the validity of the concepts of limiting fragmentation and factorization is seen in the experimental mass yield and charge distributions. Limiting fragmentation is observed in the yields of all but the light fragments ($A < 60$) for energies beginning at approximately 3.0 GeV. At 1.0 GeV the fission mass yields are similar to those at higher energies, but the yields of the heavy fragments ($145 \leq A \leq 210$) are strongly suppressed. This is consistent with the origin of the latter fragments arising from deep-spallation reactions, which can only take place if large energies were deposited during the primary interaction.

The light fragment production cross-sections are strongly increasing with energy until 8 to 12 GeV. This is indicative of the possibility that these fragments are formed in "explosive events" or are emitted from thermal sources, both of which would require large projectile energies. Comparisons of the mass yields from the ^{12}C and the ^{20}Ne-induced reactions with those previously published for proton and ^{14}N projectiles of similar energy confirm that the total projectile kinetic energy is a good parameter for describing the results of the reactions.

The theoretical model calculations give insight into the probable mechanism of formation of the various target fragments. The heavy fragments are produced by deep-spallation, in which a highly excited primary remnant evaporates a multitude of light particles. Neutron excessive fragments of fission mass ($80 < A < 145$) are produced by fission of moderately-excited near-target species. Neutron deficient fragments of this mass region are produced by fission of highly-excited heavy species and to a smaller degree by deep-spallation processes.

Of the three theoretical models, only the nuclear fireball model is clearly inferior in its predictions for the mass yield distributions, which is due to the inability of this mechanism to deposit large enough excitation energies within the fragment precursors. The nuclear firestreak and intra-nuclear cascade models both produce fair predictions for the shapes of the experimental mass and charge distributions, with the exception of the yields for the lightest fragments. This failure can be attributed to the lack of any mechanism within the de-excitation model, other than that of fission, which can populate this mass region. The two reaction models are both found to be incapable of predicting target fragment recoil velocities which are close to the previously measured values. This suggests that some other mechanism must exist for the transfer of large excitation energies to the target fragments, without the correspondingly large amounts of recoil momenta.

REFERENCES

1. J.R. Alonso, R.T. Avery, T. Elioff, R.J. Force, H.A. Grunder, H.D. Lancaster, E.J. Lofgren, J.R. Meneghetti, F.B. Selph, R.R. Stevenson, and R.B. Yourd, Science 217, 1135 (1982).

2. G.B. Yodh, Proceedings of the 1st Workshop on Ultra-Relativistic Nuclear Collisions, Lawrence Berkeley Laboratory Report LBL-8957, p. 139 (1979). See also Ref. 3.

3. A.S. Goldhaber and H.H. Heckman, Ann. Rev. Nucl. Part. Sci. 28, 161 (1978).

4. G.F. Chapline, M.H. Johnson, E. Teller, and M.S. Weiss, Phys. Rev. D8, 4302 (1973).

5. C.Y. Wong and T.A. Welton, Phys. Lett. 49B, 243 (1974).

6. R.F. Sawyer, Phys. Rev. Lett. 29, 382 (1972).

7. E.M. Friedlander, R.W. Gimpel, H.H. Heckman, Y.J. Karant, B. Judek, and E. Ganssauge, Phys. Rev. Lett. 45, 1084 (1980).

8. H.L. Bradt and B. Peters, Phys. Rev. 75, 1779 (1949).

9. R.M. DeVries and J.C. Peng, Phys. Rev. C22, 1055 (1980).

10. J. Benecke, T.T. Chou, C.N. Yang, and E. Yen, Phys. Rev. 188, 2159 (1969).

11. V.N. Gribov and I. Ya. Pomeranchuk, Phys. Rev. Lett. 8, 343 (1962).

12. D.J. Morrissey, W. Loveland, M. de Saint Simon, and G.T. Seaborg, Phys. Rev. C21, 1783 (1980).

13. J.B. Cumming, R.W. Stoenner, and P.E. Haustein, Phys. Rev. C14, 1554 (1976).

14. S.B. Kaufman, E.P. Steinberg, and M.W. Weisfield, Phys. Rev. C18, 1349 (1978).

15. P.J. Lindstrom, D.E. Greiner, H.H. Heckman, B. Cork, and F.S. Bieser, Lawrence Berkeley Laboratory Report LBL-3650 (1975).

16. G.D. Westfall, L.W. Wilson, P.J. Lindstrom, H.J. Crawford, D.E. Greiner and H.H. Heckman, Phys. Rev. C19, 1309 (1979).

17. J.B. Cumming, P.E. Haustein, and R.W. Stoenner, Phys. Rev. C10, 739 (1974).

18. J.B. Cumming, P.E. Haustein, T.J. Ruth, and G. Virtes, Phys. Rev. C17, 1632 (1978). See also J.B. Cumming, P.E. Haustein, and H.C. Hseuh, Phys. Rev. C19, 2288 (1979).

19. N.T. Porile, G.D. Cole, C.R. Rudy, Phys. Rev. C19, 2288 (1979).

20. W. Loveland, D.J. Morrissey, K. Aleklett, G.T. Seaborg, S.B. Kaufman, E.P. Steinberg, B.D. Wilkins, J.B. Cumming, P.E. Haustein, and H.C. Hseuh, Phys. Rev. C23, 253 (1981).

21. C.P. Oertel, Target Fragmentation in the Interaction of Relativistic Heavy-Ions and Protons with ^{181}Ta, M. S. thesis, Oregon State University, Sept. 1981.

22. S.B. Kaufman, E.P. Steinberg, and M.W. Weisfield, Phys. Rev. C18, 1349 (1978).

23. S.B. Kaufman, E.P. Steinberg, B.D. Wilkins, and D.J. Henderson, Phys. Rev. C22, 1897 (1980).

24. K. Aleklett, D.J. Morrissey, W. Loveland, P.L. McGaughey, and G.T. Seaborg, Phys. Rev. C23, 1044 (1981).

25. Yu-Wen Yu, Phys. Rev. C22, 933 (1980).

26. B.D. Wilkins, E.P. Steinberg, and S.B. Kaufman, Phys. Rev. C19, 856 (1979).

27. A.I. Warwick, A. Baden, H.H. Gutbrod, M.R. Maier, J. Péter, H.G. Ritter, H. Stelzer, H.H. Wieman, F. Weik, M. Freedman, D.J. Henderson, S.B. Kaufman, E.P. Steinberg, and B.D. Wilkins, Phys. Rev. Lett. 48, 1719 (1982).

28. N.T. Porile, S. Pandian, H. Klonk, C.R. Rudy, and E.P. Steinberg, Phys. Rev. C19, 1832 (1979).

29. S. Biswas and N.T. Porile, Phys. Rev. C20, 1467 (1979).

30. M. Lagarde-Simonoff and G.N. Simonoff, Phys. Rev. C20, 1498 (1979).

31. W. Loveland, R.J. Otto, D.J. Morrissey, and G.T. Seaborg, Phys. Rev. Lett. 39, 320 (1977).

32. G.D. Cole and N.T. Porile, Phys. Rev. C24, 2038 (1981).

33. See, for example, any chart of the nuclides.

34. L.C. Northcliffe and R.F Schilling, Nucl. Data Tables A7, 233 (1970).

35. T. Lund, private communication (1981).

36. D.J. Morrissey, D. Lee, R.J. Otto, and G.T. Seaborg, Nucl. Inst. Meth. 158, 499 (1979).

37. J.T. Routti and S.G. Prussin, Nucl. Inst. Meth. 72, 125 (1969).

38. I. Binder, R. Kraus, R. Klein, D. Lee, and M.M. Fowler, Lawrence Berkeley Laboratory Report LBL-6515 (1977).

39. J. Gosset, H.H. Gutbrod, W.G. Meyer, A.M. Poskanzer, A. Sandoval, R. Stock, and G.D. Westfall, Phys. Rev. C16, 629 (1977).

40. D.J. Morrissey, Study of the Role of Complete Fusion in the Reaction of ^{40}Ca and ^{56}Fe with Cerium and Terbium, Ph. D. thesis, Lawrence Berkeley Laboratory Report LBL-7713 (1978).

41. R.J. Otto, private communication (1978).

42. R. Serber, Phys. Rev. 72, 1114 (1947).

43. G.D. Westfall, J. Gosset, P.J. Johansen, A.M. Poskanzer, W.G. Meyer, H.H. Gutbrod, A. Sandoval, and R. Stock, Phys. Rev. Lett. 37, 1202 (1976).

44. W.D. Myers, Nucl. Phys. A296, 177 (1978).

45. X. Campi and J.F. Hufner, Phys. Rev. C24, 2199 (1981).

46. H. Stocker, J.A. Maruhn, and W. Greiner, Phys. Rev. Lett. 44, 725 (1980).

47. Y. Yariv and Z. Fraenkel, Phys. Rev. C20, 2227 (1979).

48. J.D. Bowman, W.J. Swiatecki, and C.F. Tsang, Lawrence Berkeley Laboratory Report LBL-2908 (1973).

49. D.J. Morrissey, W.R. Marsh, R.J. Otto, W. Loveland and G.T. Seaborg, Phys. Rev. C18, 1267 (1978).

50. L.F. Oliveira, R. Donangelo, and J.O. Rasmussen, Phys. Rev. C19, 826 (1979).

51. W.D. Myers, W.J. Swiatecki, T. Kodama, L.J. El-Jaick, and E.R. Hilf, Phys. Rev. C15, 2032 (1977).

52. J. Gosset, J.I. Kapusta, and G.D. Westfall, Phys. Rev. C18, 844 (1978).

53. I. Dostrovsky, Z. Fraenkel, and G. Friedlander, Phys. Rev. 116, 683 (1959).

54. R. Vandenbosch and J.R. Huizenga, Nuclear Fission (Academic, New York, 1973) p. 233.

55. S. Cohen and W.J. Swiatecki, Ann. Phys. 22, 406 (1963).

56. J.R. Nix, Nucl. Phys. A130, 241 (1969).

57. M. de Saint Simon, S. Haan, G. Audi, A. Coc, M. Epherre, P. Guimbal, M. Langevin, A.C. Mueller, C. Thibault, and F. Touchard, Independent Cross Sections of Na, K, Rb, Cs, and Fr Isotopes

Produced in Ta and U Targets Bombarded by ^{12}C Ions up to 77 MeV/u, submitted to Phys. Rev. C (1982).

58. H.H. Gutbrod, A.I. Warwick and H. Wieman, Lawrence Berkeley Laboratory Report LBL-14059 (1982).

59. W.D. Loveland, private communication (1982).

60. Y.Y. Chu, E.M. Franz, G. Friedlander, and P.J. Karol, Phys. Rev C4, 2202 (1971).

61. B.V. Jacak, W. Loveland, D.J. Morrissey, P.L. McGaughey, and G.T. Seaborg, Heavy Target Fragment Yields in the Interaction of 28 GeV Protons with ^{238}U, Can. J. Chem., to be published (1982).

62. H.H. Heckman, D.E. Greiner, P.J. Lindstrom, and H. Shue, Phys. Rev. C17, 1735 (1978).

63. T.A. Lasinski, A. Barbaro-Galtieri, R.L. Kelly, A. Rittenberg, A.I. Rosenfeld, T.G. Trippe, N. Barash-Schmidt, C. Bricman, V. Chaloupka, P. Soding and M. Roos, Rev. Mod. Phys. 45, S40 (1973).

64. S. Katcoff and J. Hudis, Phys. Rev. C14, 628 (1976).

65. D.J. Morrissey, L.F. Oliveira, J.O. Rasmussen, G.T. Seaborg, Y. Yariv, and Z. Fraenkel, Phys. Rev. Lett. 43, 1139 (1979).

66. W. Loveland, C. Luo, P.L. McGaughey, D.J. Morrissey, and G.T. Seaborg, Phys. Rev. C24, 464 (1981).

67. V.P. Crespo, J.B. Cumming, and J.M. Alexander, Phys. Rev. C2, 1777 (1970).

TABLE I.

Irradiation Conditions

Accel.	Beam Ion	Total kinetic energy	Total flux particles	Irrad. period min.	Target thickness mg/cm^2	Catcher material
CERN SC	$^{12}C^{4+}$	1.0 GeV	$4.34\ 10^{15}$	120.	46.8	Aluminum
Bevalac	$^{12}C^{6+}$	3.0 GeV	$8.38\ 10^{13}$	1605.	37.4,46.0	Mylar
Bevalac	$^{12}C^{6+}$	4.8 GeV	$6.23\ 10^{13}$	821.5	56.1	Mylar
Bevalac	$^{12}C^{6+}$	12 GeV	$9.13\ 10^{12}$	750.	37.1,44.8	Mylar
Bevalac	$^{20}Ne^{10+}$	5.0 GeV	$1.01\ 10^{13}$	639.8	37.2,45.8, 116.2	Mylar
Bevalac	$^{20}Ne^{10+}$	8.0 GeV	$3.76\ 10^{13}$	1074.	33.5	Mylar
Bevalac	$^{20}Ne^{10+}$	20 GeV	$1.09\ 10^{13}$	859.	25.3,63.7, 118.7	Mylar
Bevalac	$^{20}Ne^{10+}$	42 GeV	$1.93\ 10^{12}$	545.	36.0,44.6, 107.4	Mylar

TABLE II.

Charge Dispersion Parameters

Fragment mass and type	Z_{mp}	C_z	Reaction*
24 - 28 all	.405 A + 1.25	0.4	b,c,d,e,f,g,h
42 - 59 all	.405 A + 2.0	0.6	a
	.405 A + 2.0	0.8	b
	.405 A + 2.25	0.8	c,d,e,f
	.405 A + 2.25	0.9	g,h
65 - 77 all	.405 A + 2.25	0.9	a
	.405 A + 2.5	1.0	b
	.405 A + 2.5	1.1	c,d,e,f,g,h
81 - 93 n-def.	.405 A + 3.25	0.8	a,b,c,d,e,f,g,h
82 - 92 n-exc.	.405 A + 1.5	0.8	b,c,d,e,f,g,h
93 - 106 n-def.	.405 A + 3.5	0.8	a
	.405 A + 3.75	0.9	b,c,d,e,f,g,h
95 - 110 n-exc.	.405 A + 1.25	0.8	a,b,c,d,e,f,g,h
110 - 124 n-def.	.405 A + 3.0	0.9	a
	.405 A + 3.5	0.9	b,c,d,e,f,g,h
112 - 128 n-exc.	.405 A + .75	1.0	a,b,c,d,e,f,g,h
127 - 139 n-def.	.405 A + 2.75	0.9	a
	.405 A + 3.0	0.9	b,c,d,e,f,g,h
130 - 143 n-exc.	.405 A - 0.5	0.9	a
	.405 A - 1.0	0.9	b,c,d,e,f,g,h
145 - 161 all	$-.00026 A^2 + .45 A + 2.75$	0.8	a
all	$-.00026 A^2 + .45 A + 3.0$	0.8	b,c,d,e,f,g,h
166 - 175 all	$-.00026 A^2 + .45 A + 2.25$	0.8	a,b,c,d,e,f,g,h
184 - 192 all	$-.00026 A^2 + .45 A + 2.75$	0.7	b,c,d,e,f,g,h
201 - 210 all	$-.00026 A^2 + .45 A + 2.75$	0.7	a,b,c,d,e,f,g,h
230 - 237 all	$-.00026 A^2 + .45 A + 0.25$	0.6	a,b,c,d,e,f,g,h

* a, b, c, d = 1.0, 3.0, 4.8, and 12 GeV ^{12}C
e, f, g, h = 5.0, 8.0, 20, and 42 GeV ^{20}Ne

TABLE III.

ISOBARIC YIELDS (MILLIBARNS) FROM HEAVY-ION + U-238 EXPERIMENTS*

NUCLIDE	PROJECTILE							
	1 GEV C-12	3 GEV C-12	4.8 GEV C-12	12 GEV C-12	5 GEV NE-20	8 GEV NE-20	20 GEV NE-20	42 GEV NE-20
NA 24		1.533E+01 1.062E+00	3.037E+01 3.698E+00	6.062E+01 4.069E+00	5.449E+01 2.709E+00	5.419E+01 3.739E+00	7.691E+01 3.641E+00	6.413E+01 3.009E+00
MG 28		1.199E+01 4.501E-01	2.953E+01 1.309E+00	4.089E+01 2.142E+00	4.106E+01 1.198E+00	3.724E+01 1.580E+00	9.916E+01 1.366E+00	3.933E+01 1.379E+00
K 42		9.760E+00 1.767E+00	2.312E+01 4.048E+00		3.612E+01 4.308E+00	3.022E+01 3.883E+00	4.083E+01 3.191E+00	3.090E+01 6.300E+00
K 43			1.099E+01 2.938E+00		2.482E+01 2.958E+00	1.404E+01 2.482E+00	2.131E+01 3.114E+00	
SC 44M	1.492E+00 7.331E-01			1.398E+01 1.723E+00	1.430E+01 9.841E-01	1.268E+01 1.533E+00		
SC 44G		1.513E+01 3.763E+00	2.138E+01 5.349E+00				3.466E+01 5.273E+00	2.557E+01 4.061E+00
SC 46	2.464E+00 3.964E-01	1.887E+01 1.120E+00	1.874E+01 2.373E+00	2.641E+01 3.199E+00	2.874E+01 1.679E+00	3.110E+01 1.965E+00	3.698E+01 3.509E+00	
CA 47	4.560E+00 4.934E-01	8.722E+00 1.021E+00	2.062E+01 1.998E+00	1.778E+01 3.404E+00	2.709E+01 2.420E+00	2.034E+01 3.598E+00		1.972E+01 4.447E+00
SC 47			1.504E+01 1.737E+00	2.469E+01 3.477E+00	2.266E+01 2.304E+00			3.645E+01 9.908E+00
SC 48	2.610E+00 4.229E-01	8.294E+00 3.262E-01	1.713E+01 1.108E+00	1.917E+01 1.359E+00	2.300E+01 1.076E+00	2.155E+01 1.320E+00	2.535E+01 1.193E+00	1.713E+01 9.831E-01
V 48	4.555E+00 5.420E-01	9.531E+00 5.764E-01	1.249E+01 1.409E+00	2.197E+01 2.034E+00	2.382E+01 1.976E+00	2.049E+01 1.351E+00	2.361E+01 1.658E+00	2.397E+01 3.084E+00
MN 52		1.453E+01 1.013E+00	1.437E+01 2.906E+00	2.072E+01 1.004E+01	2.284E+01 3.507E+00	2.334E+01 3.345E+00	2.282E+01 2.728E+00	2.352E+01 1.198E+01
MN 56		1.515E+01 4.359E+00	1.623E+01 4.365E+00	1.148E+01 3.819E+00	2.469E+01 4.770E+00	1.369E+01 3.687E+00	2.111E+01 3.947E+00	1.596E+01 2.430E+00
FE 59	5.299E+00 3.438E-01	9.282E+00 4.383E-01	1.605E+01 1.158E+00	1.734E+01 1.795E+00	2.132E+01 1.048E+00	1.680E+01 1.229E+00	1.058E+01 3.453E+00	
ZN 65	7.665E+00 2.023E+00							
AS 71		1.222E+01 1.208E+00	2.194E+01 4.078E+00	3.481E+01 5.835E+00			4.137E+01 2.018E+00	2.842E+01 5.169E+00
ZN 72	1.840E+01 2.869E+00	2.792E+01 2.597E+00	3.404E+01 5.794E+00	3.009E+01 7.569E+00	5.279E+01 4.809E+00		4.816E+01 6.998E+00	2.435E+01 7.480E+00
GA 72		2.170E+01 1.042E+00	2.652E+01 3.123E+00	2.387E+01 3.489E+00	4.346E+01 3.485E+00	3.278E+01 7.119E+00	3.612E+01 3.995E+00	2.643E+01 4.069E+00

---

* See text,page 35.

ISOBARIC YIELDS (MILLIBARNS) FROM HEAVY-ION + U-238 EXPERIMENTS

NUCLIDE	PROJECTILE							
	1 GEV C-12	3 GEV C-12	4.8 GEV C-12	12 GEV C-12	5 GEV NE-20	8 GEV NE-20	20 GEV NE-20	42 GEV NE-20
GA 73		1.444E+01 2.744E+00	2.375E+01 7.685E+00		3.504E+01 1.062E+01	3.374E+01 6.904E+00	3.153E+01 4.973E+00	
SE 73		1.433E+01 2.147E+00	2.695E+01 3.340E+00	2.552E+01 5.904E+00	3.924E+01 6.051E+00	2.756E+01 3.380E+00		2.871E+01 2.600E+00
AS 74	1.604E+01 1.520E+00	2.311E+01 1.707E+00	2.247E+01 3.622E+00	2.906E+01 3.121E+00	4.408E+01 2.555E+00	3.207E+01 3.384E+00	3.705E+01 2.060E+00	3.067E+01 4.425E+00
SE 75	1.770E+01 1.394E+00	2.150E+01 1.614E+00		4.004E+01 1.047E+01	5.414E+01 4.425E+00	4.314E+01 3.074E+00	3.716E+01 9.785E+00	
AS 76		2.734E+01 2.474E+00	2.193E+01 2.004E+00	3.264E+01 7.974E+00	4.153E+01 5.043E+00	4.056E+01 3.935E+00	4.024E+01 6.717E+00	3.319E+01 6.332E+00
BR 77	2.323E+01 8.314E+00	2.870E+01 6.751E+00	2.813E+01 3.744E+00	3.904E+01 5.420E+00	4.526E+01 6.304E+00		3.640E+01 6.703E+00	3.628E+01 7.082E+00
RB 81				2.407E+01 3.810E+00		2.008E+01 2.195E+00	2.275E+01 6.374E+00	
SR 82	2.224E+01 3.224E+00	2.204E+01 8.464E-01	2.133E+01 1.504E+00	1.931E+01 2.094E+00	3.358E+01 1.627E+00	2.508E+01 1.475E+00	2.354E+01 1.200E+00	1.512E+01 1.873E+00
RB 82M		1.370E+01 1.703E+00	1.958E+01 2.233E+00	1.543E+01 5.274E+00	3.263E+01 4.044E+00	1.737E+01 2.468E+00	2.413E+01 2.664E+00	2.126E+01 2.374E+00
RB 83	1.234E+01 9.680E-01	1.958E+01 9.904E-01	2.374E+01 2.594E+00	2.626E+01 2.412E+00	4.490E+01 1.941E+00	3.000E+01 2.330E+00		
Y 86		2.124E+01 1.278E+00	2.305E+01 2.204E+00	2.792E+01 3.064E+00	4.094E+01 4.342E+00	3.143E+01 2.668E+00	3.920E+01 2.290E+00	2.570E+01 2.430E+00
ZR 86		1.547E+01 6.200E+00	2.206E+01 8.334E+00					
ZR 87		3.797E+01 4.241E+00			7.530E+01 1.721E+01			3.805E+01 7.404E+00
Y 87	1.564E+01 2.528E+00						3.511E+01 9.214E+00	
Y 87M		2.465E+01 1.294E+00	3.243E+01 3.025E+00	1.794E+01 4.182E+00	9.365E+01 3.416E+00	3.765E+01 4.472E+00		
ZR 88		4.568E+01 3.056E+00	7.904E+01 1.075E+01	5.404E+01 1.196E+01	8.974E+01 1.067E+01	6.044E+01 1.405E+01	7.923E+01 7.694E+00	4.452E+01 1.193E+01
Y 88		2.784E+01 1.350E+00	3.117E+01 2.718E+00	3.518E+01 3.154E+00	6.614E+01 7.387E+00	3.909E+01 3.686E+00	3.450E+01 2.412E+00	
ZR 89	1.797E+01 1.909E+00	3.044E+01 1.930E+00						

ISOBARIC YIELDS (MILLIBARNS) FROM HEAVY-ION + U-238 EXPERIMENTS

NUCLIDE	PROJECTILE							
	1 GEV C-12	3 GEV C-12	4.8 GEV C-12	12 GEV C-12	5 GEV NE-20	8 GEV NE-20	20 GEV NE-20	42 GEV NE-20
ZR 89	1.432E+01 1.533E+00	2.364E+01 1.237E+00	3.299E+01 2.744E+00	3.499E+01 3.294E+00	5.120E+01 2.323E+00	3.531E+01 2.775E+00	4.088E+01 2.638E+00	3.259E+01 1.764E+00
Y 90M		6.157E+01 5.056E+00	6.588E+01 8.174E+00	6.364E+01 9.713E+00	1.284E+02 8.451E+00	7.341E+01 8.373E+00	7.511E+01 6.923E+00	5.817E+01 1.055E+01
SR 91		5.293E+01 2.979E+00	5.423E+01 4.777E+00	5.078E+01 4.608E+00	9.416E+01 4.772E+00	6.859E+01 4.895E+00	6.993E+01 4.229E+00	5.459E+01 4.855E+00
SR 92		6.983E+01 5.633E+00	7.439E+01 7.783E+00	7.133E+01 1.049E+01	1.261E+02 1.113E+01	9.238E+01 8.309E+00	9.220E+01 9.583E+00	7.845E+01 9.169E+00
Y 92		6.129E+01 5.799E+00	6.954E+01 1.237E+01	5.499E+01 9.743E+00		6.576E+01 8.471E+00	7.297E+01 1.568E+01	
MO 93M		1.517E+01 1.169E+00	1.899E+01 1.693E+00	1.834E+01 2.571E+00	3.968E+01 2.773E+00	2.214E+01 1.928E+00	2.857E+01 2.319E+00	1.919E+01 1.829E+00
TC 93		1.714E+01 3.578E+00			3.389E+01 1.243E+01	3.068E+01 9.683E+00	3.707E+01 1.303E+01	2.997E+01 1.517E+01
TC 94			1.291E+01 2.134E+00				2.210E+01 2.362E+00	1.540E+01 8.308E+00
ZR 95	4.214E+01 2.740E+00	5.092E+01 2.079E+00	5.527E+01 5.208E+00	4.898E+01 3.117E+00	8.771E+01 3.294E+00	7.145E+01 4.291E+00	5.960E+01 3.014E+00	4.975E+01 5.707E+00
TC 95		1.413E+01 1.217E+00	1.756E+01 1.494E+00	1.894E+01 2.383E+00	3.005E+01 5.549E+00	2.018E+01 1.734E+00	2.565E+01 1.394E+00	1.653E+01 1.779E+00
NB 96	4.343E+01 6.604E+00	5.134E+01 1.571E+00	4.384E+01 2.589E+00	4.844E+01 2.322E+00	7.930E+01 2.829E+00	6.037E+01 3.522E+00	5.369E+01 2.403E+00	
TC 96	1.081E+01 1.003E+00	1.404E+01 1.004E+00	1.652E+01 1.565E+00	1.663E+01 2.142E+00	2.730E+01 1.339E+00	2.030E+01 1.961E+00	1.919E+01 1.520E+00	1.278E+01 1.885E+00
ZR 97		6.662E+01 4.369E+00	8.311E+01 6.351E+00	6.528E+01 7.857E+00	1.027E+02 8.754E+00	9.648E+01 8.510E+00	9.094E+01 8.564E+00	7.346E+01 1.029E+01
RU 97	9.801E+00 2.962E+00	1.356E+01 1.107E+00		2.037E+01 3.295E+00	2.989E+01 2.619E+00	2.378E+01 2.653E+00	2.890E+01 3.394E+00	2.074E+01 2.056E+00
MO 99	3.752E+01 2.461E+00	4.996E+01 2.310E+00	3.676E+01 4.604E+00	5.404E+01 4.153E+00	9.332E+01 4.598E+00	6.470E+01 3.932E+00	6.109E+01 2.991E+00	4.838E+01 5.858E+00
RH 99M				1.515E+01 2.780E+00	2.779E+01 2.568E+00			
RH 99X						1.549E+01 3.792E+00		
RH100	1.139E+01 1.672E+00	1.221E+01 9.298E-01	1.301E+01 1.302E+00	1.470E+01 5.234E+00	3.159E+01 2.030E+00	1.922E+01 1.808E+00	2.221E+01 1.875E+00	1.819E+01 1.541E+00

ISOBARIC YIELDS (MILLIBARNS) FROM HEAVY-ION + U-238 EXPERIMENTS

NUCLIDE	PROJECTILE 1 GEV C-12	3 GEV C-12	4.8 GEV C-12	12 GEV C-12	5 GEV NE-20	8 GEV NE-20	20 GEV NE-20	42 GEV NE-20
RH101M	1.109E+01 1.515E+00	1.503E+01 1.170E+00	2.239E+01 1.947E+00	2.370E+01 2.233E+00		1.912E+01 2.570E+00	2.012E+01 1.965E+00	2.240E+01 2.133E+00
RU103	8.246E+01 5.095E+00	9.593E+01 3.677E+00	8.487E+01 7.809E+00	9.730E+01 8.509E+00	1.362E+02 6.617E+00	1.171E+02 5.879E+00	1.103E+02 9.403E+00	9.151E+01 8.013E+00
RU105		5.771E+01 2.590E+00	5.090E+01 3.995E+00	5.064E+01 2.097E+00	1.020E+02 9.644E+00	6.860E+01 4.990E+00	6.830E+01 3.676E+00	5.101E+01 3.797E+00
RH105	7.540E+01 1.173E+01		8.539E+01 8.969E+00	8.873E+01 6.782E+00	1.751E+02 8.389E+00	1.110E+02 1.534E+01	1.161E+02 7.289E+00	8.142E+01 8.423E+00
AG105	1.993E+01 2.074E+00	1.792E+01 1.139E+00						
AG106M	1.134E+01 5.023E-01	1.216E+01 4.695E-01				1.362E+01 9.551E-01		
AG110M	6.160E+01 3.014E+00	9.260E+01 5.970E+00	4.037E+01 1.474E+01	6.291E+01 2.509E+01	9.261E+01 1.391E+01	7.464E+01 7.951E+00		
IN110M				1.474E+01 3.921E+00	3.543E+01 4.387E+00	2.120E+01 2.951E+00	2.502E+01 4.291E+00	
CD111M		2.309E+01 4.634E+00		1.047E+01 5.537E+00			2.730E+01 1.163E+01	
IN111	1.063E+01 2.500E+00	1.763E+01 9.613E-01	2.049E+01 1.970E+00	2.194E+01 1.440E+00	3.394E+01 1.902E+00	2.573E+01 4.523E+00	2.776E+01 1.414E+00	1.966E+01 1.283E+00
PD112		7.697E+01 4.473E+00	8.760E+01 6.562E+00	1.066E+02 9.851E+00	1.510E+02 8.107E+00	1.350E+02 1.920E+01	1.380E+02 1.108E+01	1.069E+02 9.334E+00
IN114M	2.183E+01 1.969E+00							
CD117M				8.251E+01 2.604E+01				8.546E+01 2.779E+01
SN117M	1.292E+01 1.339E+00	1.159E+01 8.769E-01						2.657E+01 3.234E+00
SB118M		1.540E+01 7.349E-01	1.480E+01 1.090E+00		2.614E+01 1.732E+00	1.553E+01 9.907E-01	1.552E+01 1.447E+00	
SB120M	2.112E+01 2.361E+00	2.991E+01 2.746E+00			4.412E+01 4.734E+00	3.301E+01 7.955E+00	3.701E+01 3.533E+00	
TE121		1.327E+01 8.470E-01	1.190E+01 1.310E+00	1.626E+01 1.730E+00	2.274E+01 1.597E+00	1.665E+01 2.569E+00	1.742E+01 1.174E+00	1.826E+01 3.739E+00
TE121M	1.629E+01 1.879E+00							

ISOBARIC YIELDS (MILLIBARNS) FROM HEAVY-ION + U-238 EXPERIMENTS

NUCLIDE	PROJECTILE							
	1 GEV C-12	3 GEV C-12	4.8 GEV C-12	12 GEV C-12	5 GEV NE-20	8 GEV NE-20	20 GEV NE-20	42 GEV NE-20
I 121		2.031E+01 4.723E+00	1.690E+01 2.369E+00	2.490E+01 3.769E+00	3.660E+01 4.090E+00	2.401E+01 3.949E+00		1.803E+01 1.792E+00
SB122	3.490E+01 4.076E+00	4.007E+01 2.584E+00	2.403E+01 2.904E+00	3.391E+01 3.107E+00	6.007E+01 7.479E+00	3.920E+01 7.130E+00	3.611E+01 3.804E+00	3.137E+01 3.667E+00
TE123M	1.940E+01 4.530E+00							
I 123		1.591E+01 2.912E+00	1.018E+01 1.208E+00	2.390E+01 4.634E+00	3.787E+01 6.751E+00	2.791E+01 7.112E+00	2.904E+01 3.014E+00	2.392E+01 4.071E+00
SB124	2.490E+01 1.589E+00	2.744E+01 1.194E+00	2.477E+01 2.639E+00	2.256E+01 2.580E+00	4.492E+01 1.953E+00	3.491E+01 1.326E+00	2.087E+01 2.183E+00	
I 124	1.834E+01 2.086E+00	2.154E+01 1.108E+00	1.544E+01 2.001E+00	1.509E+01 2.221E+00	3.294E+01 2.271E+00	2.219E+01 2.025E+00	2.019E+01 1.905E+00	1.491E+01 2.046E+00
SN125	2.682E+01 3.234E+00	3.317E+01 2.458E+00	3.918E+01 7.680E+00		5.734E+01 1.108E+01	4.759E+01 1.093E+01		
SB126	2.207E+01 1.281E+00	2.234E+01 7.387E-01	1.959E+01 1.933E+00		3.376E+01 1.431E+00	2.894E+01 1.728E+00	2.494E+01 1.201E+00	
SB127	3.794E+01 3.013E+00	4.077E+01 2.194E+00	4.718E+01 3.423E+00	4.698E+01 4.137E+00	8.487E+01 3.684E+00	6.171E+01 5.168E+00	6.456E+01 3.227E+00	4.791E+01 4.425E+00
XE127	2.177E+01 1.413E+00	1.804E+01 9.949E-01		1.783E+01 3.709E+00	3.373E+01 3.733E+00	2.354E+01 1.903E+00		
CS127			2.876E+01 2.798E+00	3.227E+01 4.297E+00	5.076E+01 4.317E+00		4.163E+01 3.713E+00	
SB128		2.804E+01 3.591E+00	3.233E+01 2.682E+00	2.254E+01 3.909E+00	6.133E+01 3.965E+00	2.929E+01 1.004E+01	4.308E+01 3.492E+00	3.019E+01 6.216E+00
BA128	1.499E+01 3.683E+00	1.853E+01 2.308E+00	1.932E+01 5.354E+00	2.043E+01 2.233E+00	3.126E+01 4.652E+00	2.802E+01 6.974E+00	3.116E+01 8.039E+00	
CS129		2.603E+01 1.343E+00	2.162E+01 2.253E+00	2.904E+01 3.439E+00	4.463E+01 4.284E+00	3.049E+01 3.769E+00	3.322E+01 3.063E+00	
I 130		4.352E+01 2.258E+00	4.543E+01 3.578E+00	2.314E+01 2.741E+00	8.758E+01 6.353E+00	4.136E+01 3.325E+00	6.304E+01 4.400E+00	3.168E+01 4.701E+00
I 131	2.415E+01 1.879E+00	3.062E+01 1.617E+00	3.409E+01 4.102E+00	3.141E+01 3.603E+00	5.428E+01 2.412E+00	3.992E+01 3.600E+00	4.269E+01 3.020E+00	3.332E+01 2.781E+00
BA131	2.793E+01 1.068E+00	2.899E+01 1.561E+00	2.652E+01 2.598E+00	3.130E+01 4.180E+00	5.616E+01 4.299E+00	2.977E+01 1.694E+00	2.732E+01 2.052E+00	
TE132	2.701E+01 1.313E+00	2.869E+01 8.598E-01	2.488E+01 1.579E+00	2.673E+01 1.654E+00	3.530E+01 2.200E+00	3.147E+01 1.802E+00	3.422E+01 1.604E+00	2.901E+01 2.327E+00

ISOBARIC YIELDS (MILLIBARNS) FROM HEAVY-ION + U-238 EXPERIMENTS

NUCLIDE	PROJECTILE							
	1 GEV C-12	3 GEV C-12	4.8 GEV C-12	12 GEV C-12	5 GEV NE-20	8 GEV NE-20	20 GEV NE-20	42 GEV NE-20
I 132		2.297E+01 2.285E+00	3.199E+01 5.959E+00		7.334E+01 2.011E+01	3.577E+01 4.182E+00	2.538E+01 3.654E+00	1.959E+01 2.607E+00
CE132		3.177E+01 7.645E+00				3.208E+01 1.227E+01		
I 133		2.420E+01 1.269E+00	2.011E+01 1.691E+00	2.610E+01 3.157E+00	4.560E+01 2.595E+00	2.282E+01 4.810E+00	3.953E+01 1.905E+00	3.300E+01 2.820E+00
CE133		1.675E+01 2.779E+00	1.775E+01 1.874E+00	1.697E+01 3.937E+00	3.382E+01 9.291E+00	2.119E+01 4.501E+00	3.199E+01 4.298E+00	1.825E+01 3.355E+00
I 134		3.509E+01 4.864E+00			5.829E+01 1.290E+01	4.905E+01 7.883E+00	3.724E+01 7.585E+00	4.328E+01 6.531E+00
CS134	1.050E+01 2 393E+00							
I 135		3.233E+01 1.949E+00	3.728E+01 2.348E+00	3.601E+01 4.579E+00	6.264E+01 5.895E+00	3.869E+01 3.268E+00	5.228E+01 3.124E+00	4.730E+01 4.823E+00
XE135				3.048E+01 6.130E+00	6.327E+01 8.226E+00			3.384E+01 6.552E+00
CE135		1.209E+01 1.463E+00	1.593E+01 4.203E+00	1.634E+01 1.567E+00	2.633E+01 2.575E+00	1.495E+01 1.919E+00	1.709E+01 2.511E+00	1.387E+01 4.180E+00
CS136	1.238E+01 6.092E-01	2.109E+01 8.746E-01	1.998E+01 1.608E+00	1.513E+01 2.121E+00	3.891E+01 1.843E+00	2.531E+01 1.807E+00	2.135E+01 2.137E+00	
BA139				2.475E+01 6.031E+00	2.472E+01 5.208E+00			2.016E+01 5.313E+00
CE139	1.401E+01 1.320E+00							
BA140	1.586E+01 1.338E+00	1.634E+01 1.081E+00		2.108E+01 1.276E+00	3.381E+01 9.827E-01	2.819E+01 2.212E+00	2.928E+01 4.164E+00	2.644E+01 3.107E+00
LA142		1.578E+01 6.895E+00			2.529E+01 8.075E+00			1.902E+01 7.547E+00
CE143	1.849E+01 1.398E+00	1.298E+01 8.824E-01	1.277E+01 1.872E+00	1.233E+01 2.269E+00	2.689E+01 1.896E+00	1.535E+01 2.486E+00	1.994E+01 1.105E+00	1.548E+01 1.993E+00
EU145	4.308E+00 4.898E-01	1.298E+01 5.938E-01	1.491E+01 1.152E+00	1.462E+01 1.321E+00	2.059E+01 1.052E+00	1.598E+01 1.034E+00	1.718E+01 1.680E+00	
EU147	4.816E+00 6.086E-01	2.124E+01 1.684E+00	1.926E+01 7.529E+00			3.177E+01 4.677E+00	3.883E+01 1.680E+01	
GD147		1.366E+01 1.694E+00	1.504E+01 1.447E+00	2.104E+01 3.720E+00	2.761E+01 4.629E+00	1.694E+01 1.179E+00	3.376E+01 3.391E+00	2.066E+01 1.858E+00

ISOBARIC YIELDS (MILLIBARNS) FROM HEAVY-ION + U-238 EXPERIMENTS

NUCLIDE	PROJECTILE 1 GEV C-12	3 GEV C-12	4.8 GEV C-12	12 GEV C-12	5 GEV NE-20	8 GEV NE-20	20 GEV NE-20	42 GEV NE-20
EU148	3.619E+00 4.619E-01							
GD149	3.008E+00 9.140E-01	1.861E+01 7.880E-01	9.682E+00 1.419E+00	1.212E+01 1.194E+00	1.894E+01 1.172E+00	1.195E+01 1.055E+00		
TB151		2.040E+01 2.182E+00	1.694E+01 2.214E+00		3.200E+01 2.743E+00	1.140E+01 4.632E+00	3.194E+01 3.244E+00	2.141E+01 4.584E+00
DY153				8.150E+00 3.360E+00	1.387E+01 5.407E+00		1.089E+01 2.472E+00	
HO156		8.418E+00 2.704E+00					1.810E+01 3.622E+00	
DY157		1.204E+01 1.314E+00	1.318E+01 1.635E+00	1.453E+01 1.914E+00	2.157E+01 2.597E+00	1.609E+01 1.777E+00	1.840E+01 2.490E+00	1.475E+01 1.286E+00
ER161		9.968E+00 1.232E+00		1.404E+01 5.004E+00			1.692E+01 2.173E+00	1.109E+01 1.886E+00
YB166	3.512E+00 6.672E-01	1.470E+01 1.088E+00	1.461E+01 1.507E+00	1.493E+01 3.263E+00	2.494E+01 1.788E+00		2.207E+01 4.533E+00	1.346E+01 2.596E+00
YB169	2.865E+00 1.251E+00	1.918E+01 8.491E-01			1.909E+01 1.341E+00	1.342E+01 1.011E+00		
LU169		1.150E+01 1.039E+00					2.293E+01 4.847E+00	
LU170		9.694E+00 6.870E-01				1.234E+01 2.316E+00		
HF170			1.251E+01 1.979E+00	1.901E+01 6.753E+00	2.855E+01 4.074E+00		2.527E+01 2.534E+00	1.595E+01 3.300E+00
LU171			1.260E+01 1.523E+00	2.021E+01 4.432E+00	2.563E+01 5.195E+00	8.610E+00 2.173E+00	1.954E+01 3.271E+00	
HF173		8.292E+00 8.466E-01	1.058E+01 1.326E+00	1.422E+01 3.[illegible]E+00		1.030E+01 8.243E-01	1.184E+01 1.145E+00	
HF175	3.207E+00 1.065E+00							
IR184		7.132E+00 1.897E+00						6.647E+00 2.421E+00
AU192						1.113E+01 1.360E+00	2.000E+01 2.647E+00	
HG192		7.098E+00 1.043E+00	9.032E+00 1.414E+00	7.731E+00 1.222E+00	1.335E+01 2.495E+00	7.461E+00 9.876E-01	1.126E+01 3.515E+00	

ISOBARIC YIELDS (MILLIBARNS) FROM HEAVY-ION + U-238 EXPERIMENTS

NUCLIDE	PROJECTILE							
	1 GEV C-12	3 GEV C-12	4.8 GEV C-12	12 GEV C-12	5 GEV NE-20	8 GEV NE-20	20 GEV NE-20	42 GEV NE-20
PB201		3.238E+00 3.952E-01		5.262E+00 7.375E-01	6.398E+00 1.022E+00		7.279E+00 6.899E-01	4.992E+00 6.162E-01
BI202		4.731E+00 7.334E-01	7.784E+00 1.626E+00	6.306E+00 1.413E+00	9.036E+00 1.667E+00	7.567E+00 1.229E+00	1.027E+01 2.689E+00	6.937E+00 1.342E+00
PB203			9.316E+00 1.101E+00		9.800E+00 1.478E+00	7.933E+00 7.846E-01		
BI204		5.629E+00 3.627E-01	7.338E+00 8.634E-01	6.794E+00 7.434E-01	1.070E+01 1.109E+00	6.938E+00 7.266E-01	1.308E+01 1.306E+00	6.796E+00 6.623E-01
BI205	3.377E+00 2.151E-01	9.419E+00 5.919E-01	1.178E+01 1.061E+00		9.149E+00 1.619E+00	1.126E+01 1.306E+00	1.934E+01 2.438E+00	
BI206						1.169E+01 2.343E+00	1.094E+01 5.140E+00	
PO206	2.264E+00 2.795E-01	5.969E+00 3.279E-01	6.935E+00 9.041E-01	6.150E+00 6.708E-01	8.567E+00 3.548E-01	8.049E+00 7.641E-01	1.015E+01 9.552E-01	8.507E+00 1.421E+00
PO207		4.099E+00 6.997E-01	5.489E+00 9.113E-01		7.621E+00 1.084E+00	8.491E+00 1.402E+00		6.287E+00 1.686E+00
AT209		7.256E+00 6.098E-01	8.149E+00 6.388E-01	7.321E+00 1.528E+00	1.694E+01 1.938E+00	1.219E+01 7.972E-01	1.142E+01 1.168E+00	8.726E+00 1.296E+00
AT210		7.216E+00 3.871E-01	1.054E+01 8.992E-01	8.045E+00 1.047E+00	1.305E+01 2.251E+00	1.058E+01 1.018E+00	1.479E+01 1.795E+00	1.026E+01 1.386E+00
PA230	6.305E+00 6.968E-01	1.366E+01 1.032E+[illegible]			1.857E+01 4.348E+00	1.594E+01 4.271E+00		
PA232	4.985E+00 1.645E+00	1.589E+01 1.061E+00	1.819E+01 2.070E+00	1.808E+01 3.464E+00	2.773E+01 1.536E+00	2.343E+01 2.226E+00	1.839E+01 1.917E+00	2.043E+01 1.784E+00
PA233	8.257E+00 6.945E-01	1.808E+01 1.038E+00	2.223E+01 2.081E+00	2.131E+01 2.193E+00	3.130E+01 1.616E+00	2.904E+01 2.067E+00	2.029E+01 2.261E+00	2.435E+01 3.140E+00
PA234		3.262E+01 2.588E+00		3.105E+01 3.785E+00	5.848E+01 4.752E+00	3.962E+01 3.702E+00	4.181E+01 6.319E+00	3.552E+01 2.923E+00
U 237	1.517E+02 1.181E+01	2.020E+02 1.071E+01	2.298E+02 1.439E+01	2.675E+02 3.010E+01	4.204E+02 2.271E+01		3.680E+02 5.866E+01	3.986E+02 2.777E+01

TABLE IV.

Total Reaction and Fission Cross-sections
for Heavy-ions and Protons with ^{238}U
(barns)

Projectile	reaction	fission	Fraction	INC reaction	Firestreak reaction
1.0 GeV ^{12}C	2.31	1.65	.71	3.34	3.15
3.0	3.33	2.03	.61	3.36	3.41
4.8	3.71	2.00	.54	3.44	3.51
12.	4.08	2.18	.53	3.54	3.71
5.0 GeV ^{20}Ne	6.36	3.59	.56	3.52	3.84
8.0	4.33	2.65	.61	3.86	3.96
20.	5.02	2.76	.55	3.96	4.15
42.	4.24	2.26	.53	----	4.35
11-29 GeV p	1.84	1.06	.58		
2.0 GeV ^{14}N	----	2.84	---		
3.9	----	2.39	---		
29.	----	2.13	---		

The values shown for 11-29 GeV protons were computed using the data from Reference 25. The fission cross-sections for the ^{14}N-induced reactions were taken from Reference 64.

FIGURE CAPTIONS

(1) A typical Bevalac targetry arrangement.

(2) The schematic diagram of a conventional gamma-ray spectroscopy system.

(3A-3B) The flowchart diagram for the sequence of computer operations used in the analysis of the gamma-ray spectra.

(4-19) The independent yield distributions from the reaction of 3.0 GeV ^{12}C with ^{238}U. The plotted points are the experimental values and the solid lines are the fitted Gaussian charge distributions.

(20-27) The mass yield distributions for the eight reactions studied. The open circles are the total (isobaric) yields, while the triangles are the total neutron excessive yields and the squares are the total neutron deficient yields. The solid lines are the fitted isobaric yield curves.

(28) A comparison of the mass yield curves for ^{12}C induced reactions. The curves A, B, C, and D represent total projectile kinetic energies of 1.0, 3.0, 4.8 and 12 GeV, respectively.

(29) A comparison of the mass yield curves for ^{20}Ne induced reactions. The curves A, B, C, and D represent total projectile kinetic energies of 5.0, 8.0, 20, and 42 GeV, respectively.

(30) A comparison of the mass yield curves for the 4.8 GeV ^{12}C and

5.0 GeV ^{20}Ne induced reactions, labeled as A and B, respectively.

(31) A comparison of the mass yield curves for the 28 GeV proton and 20 GeV ^{20}Ne induced reactions, labeled as A and B, respectively. The data for the proton induced reaction were taken from Reference 60.

(32-38) The mass yield distributions predicted by the various theoretical models are compared with the experimental results. The solid lines are the experimental curves, while the curves labeled as A, B, and C correspond to the intra-nuclear cascade, nuclear firestreak, and nuclear fireball model calculations.

(39) A comparison of the experimental and theoretical mass yield curves for the reaction of 42 GeV ^{20}Ne with ^{238}U. The solid curve is the experimental data and the curve labeled A is the nuclear firestreak model prediction.

(40) A comparison of the independent yields for fragments with mass numbers 30 to 50, produced in the reaction of 3.0 GeV ^{12}C with ^{238}U, and the charge distributions predicted by the intra-nuclear cascade model. The plotted points are the experimental data and the solid curve is the result of the model calculation.

(41) A comparison of the theoretical and experimental target fragment longitudinal velocities imparted during the reaction of 4.8 GeV ^{12}C with ^{238}U. The plotted points are the

experimental data for the neutron deficient fragments, which were taken from Reference 66. The solid curves are the velocities for the fragments not arising from fission, as predicted by the intra-nuclear cascade and nuclear firestreak model calculations.

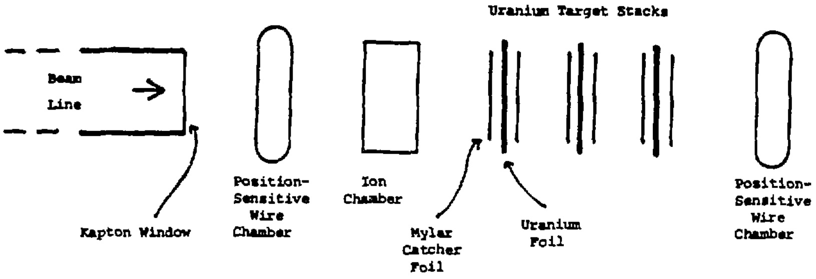
Uranium Target Stacks
Beam
Line
Kapton Window
Position-Sensitive Wire Chamber
Ion Chamber
Mylar Catcher Foil
Uranium Foil
Position-Sensitive Wire Chamber

Figure 1.

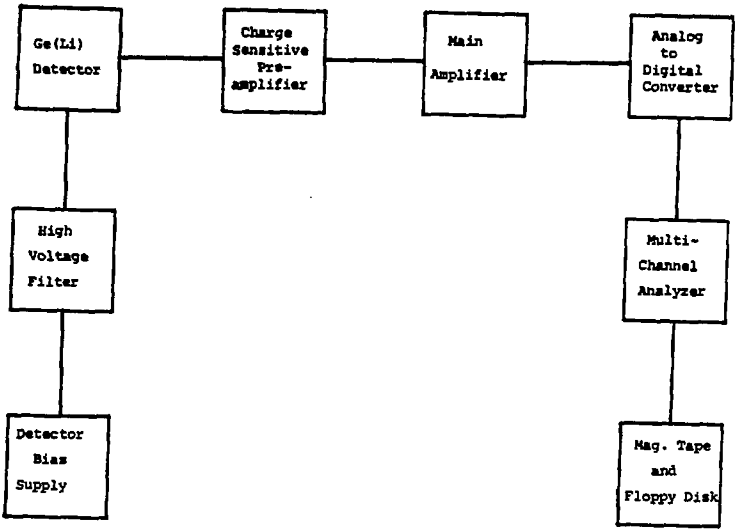
Ge(Li) Detector
Charge Sensitive Pre-amplifier
Main Amplifier
Analog to Digital Converter
High Voltage Filter
Multi-Channel Analyzer
Detector Bias Supply
Mag. Tape and Floppy Disk

Figure 2.

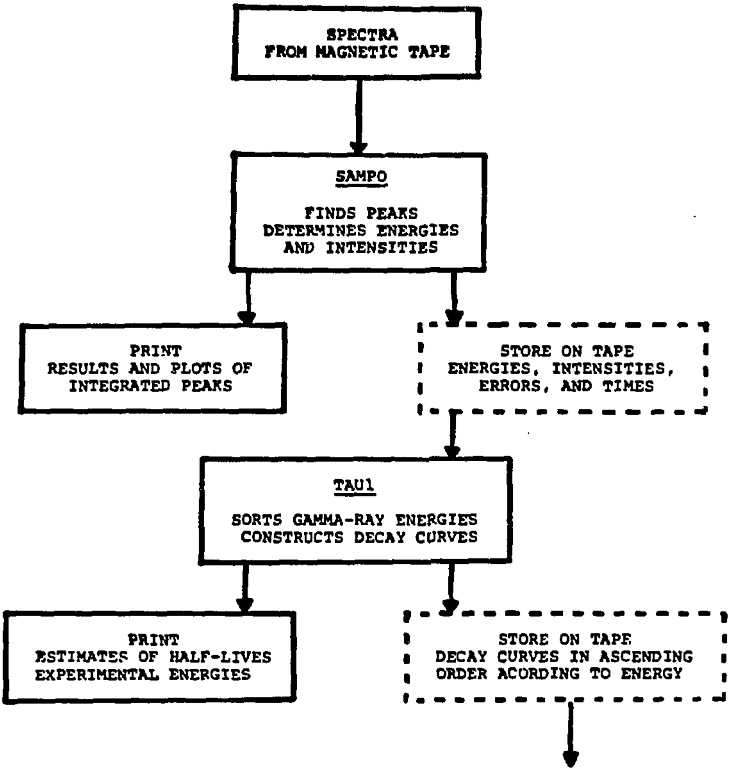

(A) AUTOMATIC MODE: PHOTOPEAK ANALYSIS, AND DECAY CURVE CONSTRUCTION

FIGURE 3A.

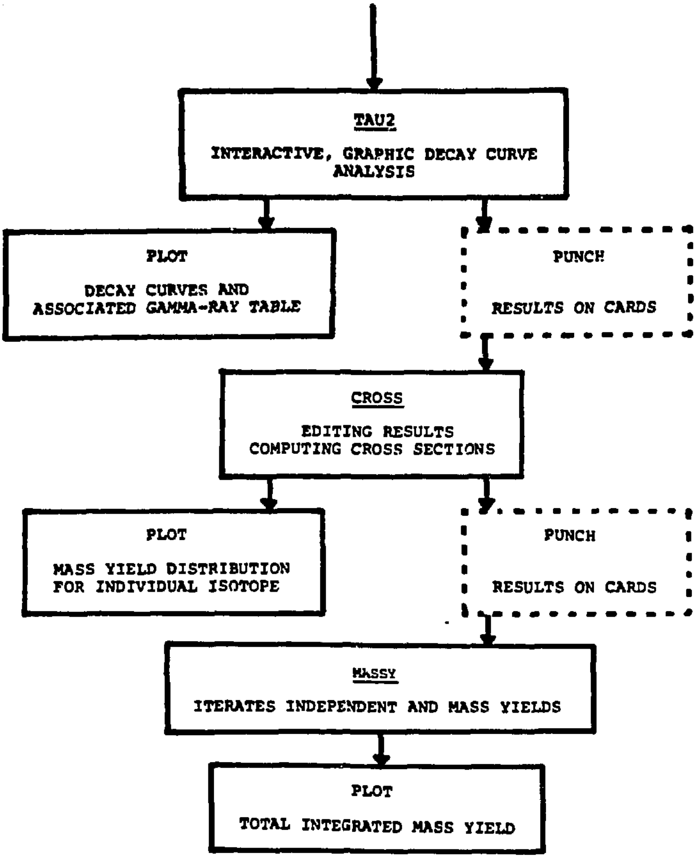

(B) INTERACTIVE MODE: DECAY CURVE ANALYSIS, AND A TOTAL CROSS SECTIONAL YIELD CALCULATION

FIGURE 3B.

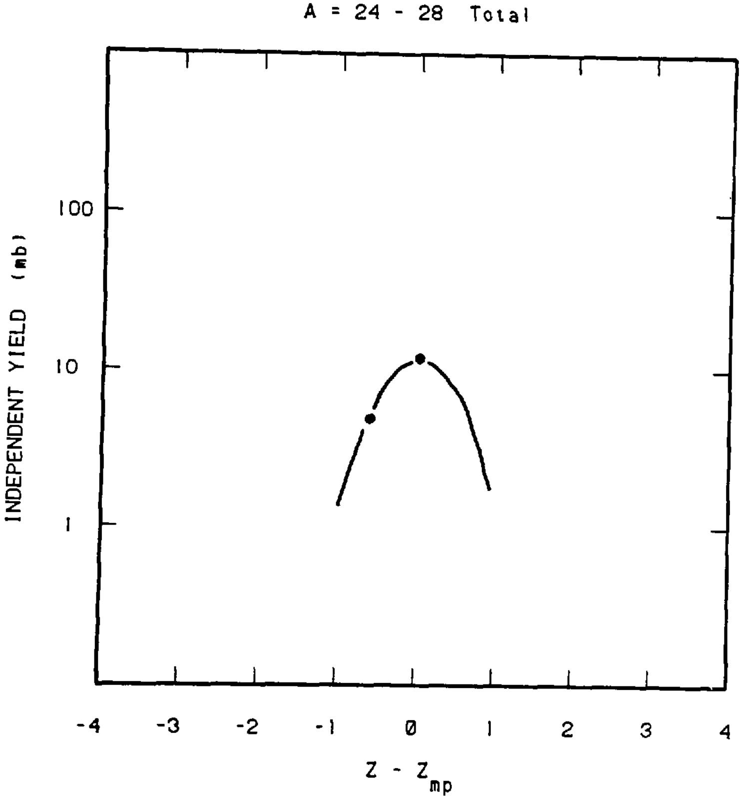

FIGURE 4.

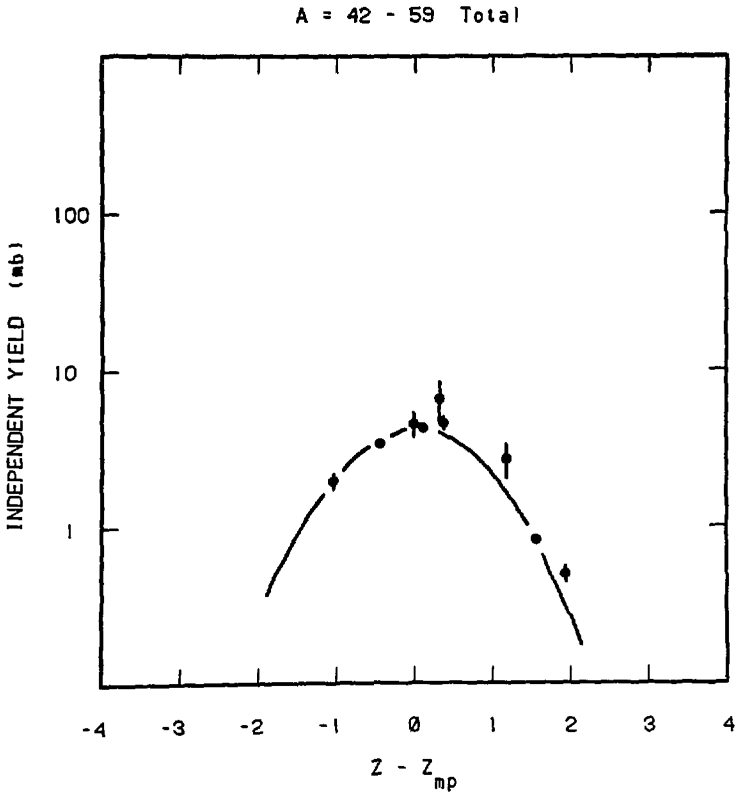

FIGURE 5.

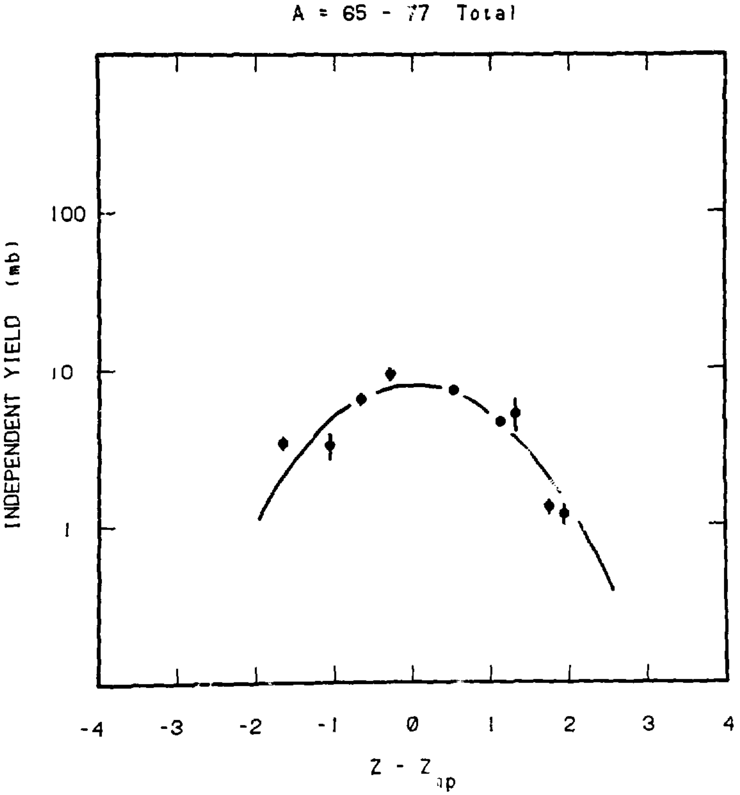

FIGURE 6.

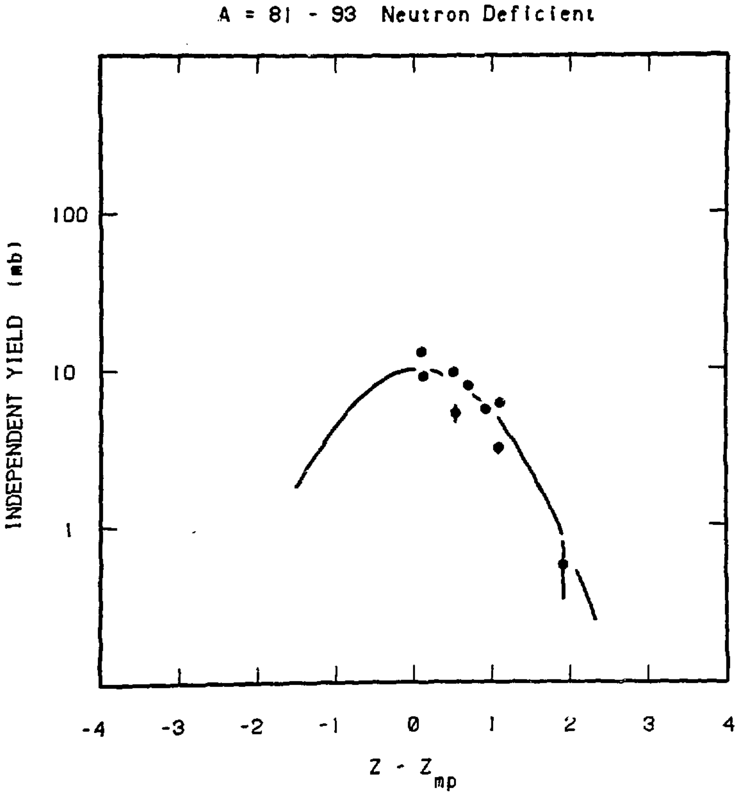
A = 81 - 93 Neutron Deficient
INDEPENDENT YIELD (mb)
100
10
1
-4
-3
-2
-1
0
1
2
3
4
Z - Z_{mp}

FIGURE 7.

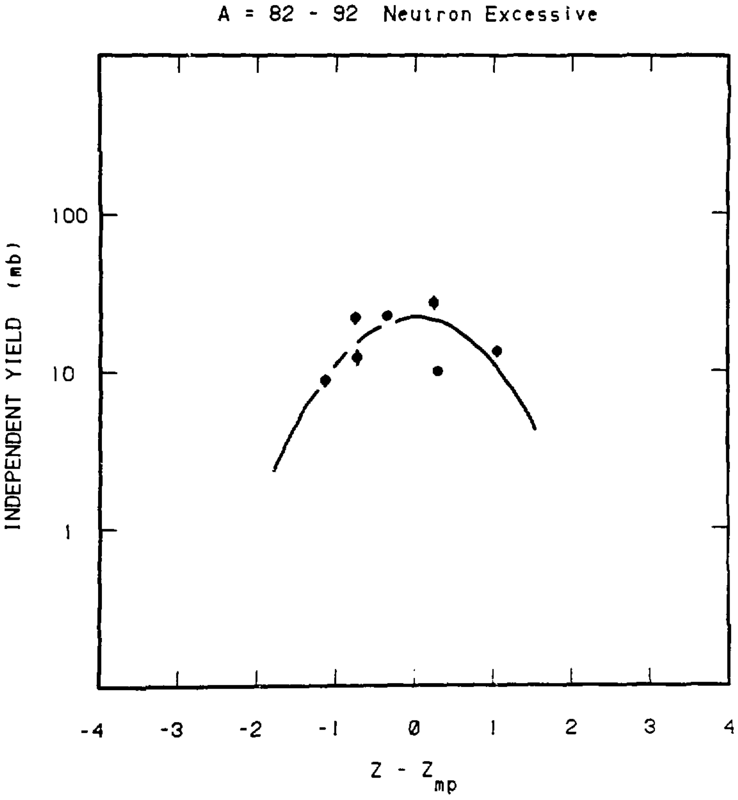
A = 82 - 92 Neutron Excessive
INDEPENDENT YIELD (mb)
100
10
1
-4
-3
-2
-1
0
1
2
3
4
Z - Z_{mp}

FIGURE 8.

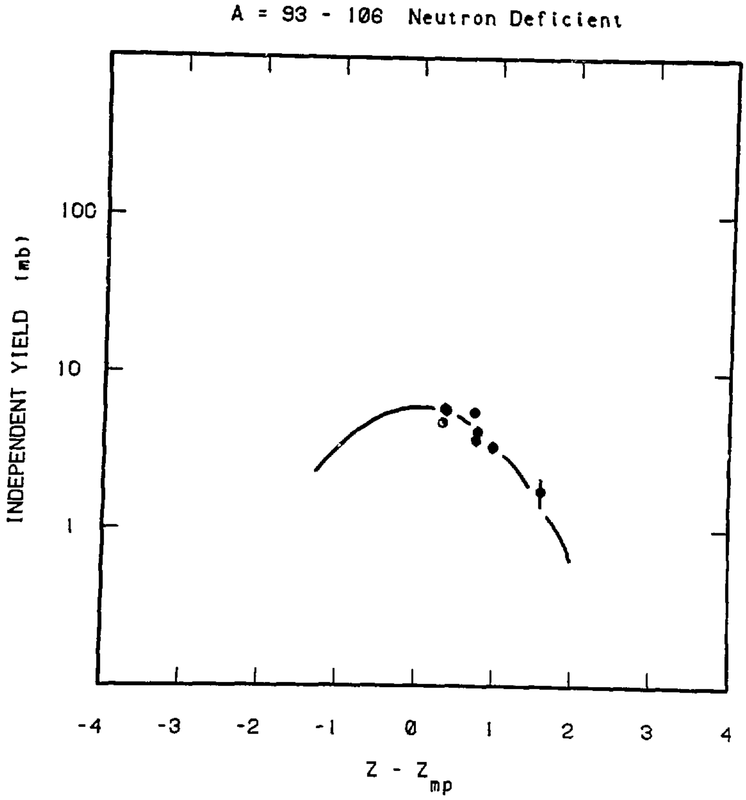
A = 93 - 106 Neutron Deficient
INDEPENDENT YIELD (mb)
100
10
1
-4
-3
-2
-1
0
1
2
3
4
Z - Z mp

FIGURE 9.

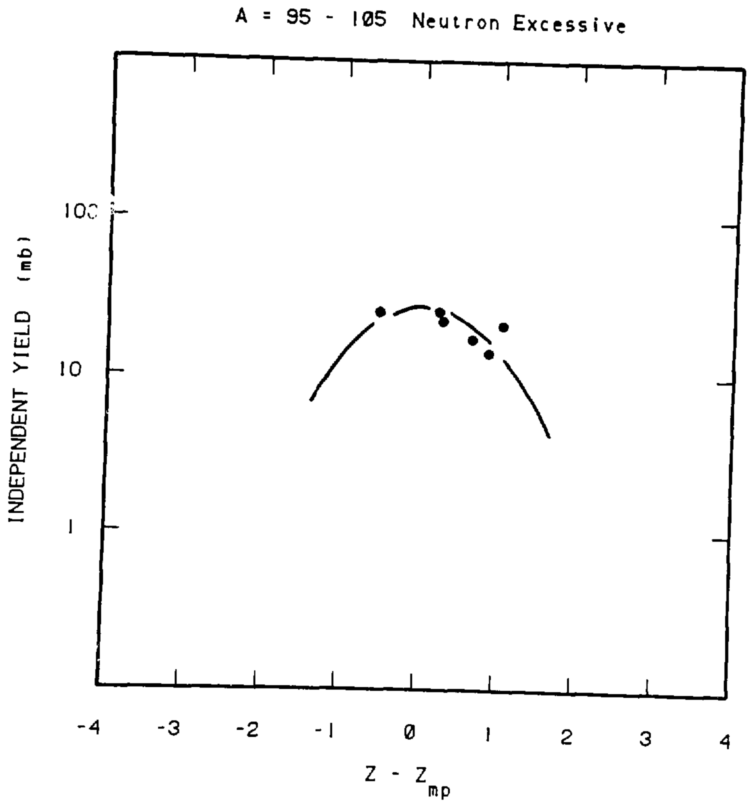
A = 95 - 105 Neutron Excessive
INDEPENDENT YIELD (mb)
100
10
1
-4
-3
-2
-1
0
1
2
3
4
Z - Z_{mp}

FIGURE 10.

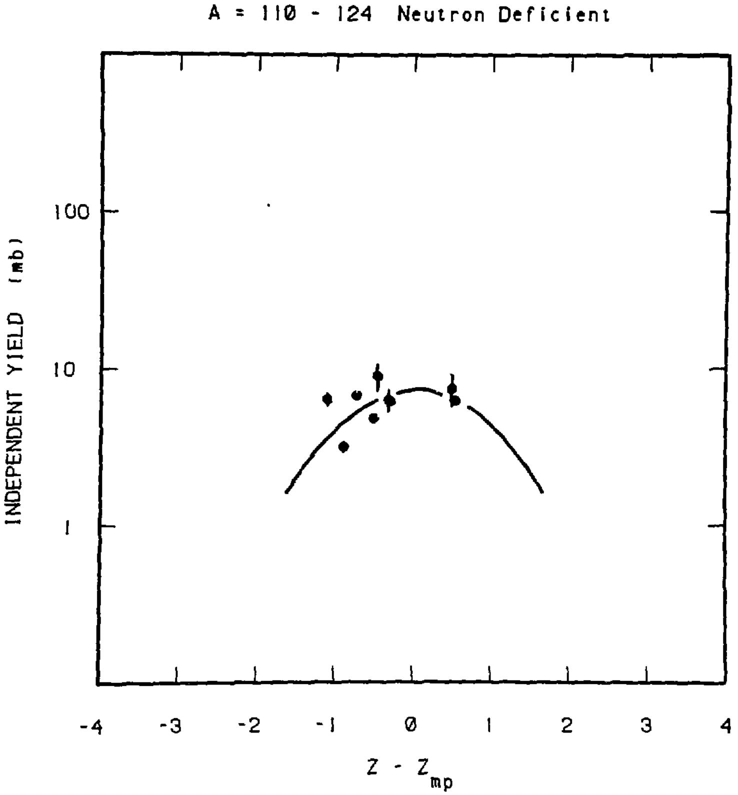
A = 110 - 124 Neutron Deficient
INDEPENDENT YIELD (mb)
100
10
1
-4
-3
-2
-1
0
1
2
3
4
Z - Z_{mp}

FIGURE 11.

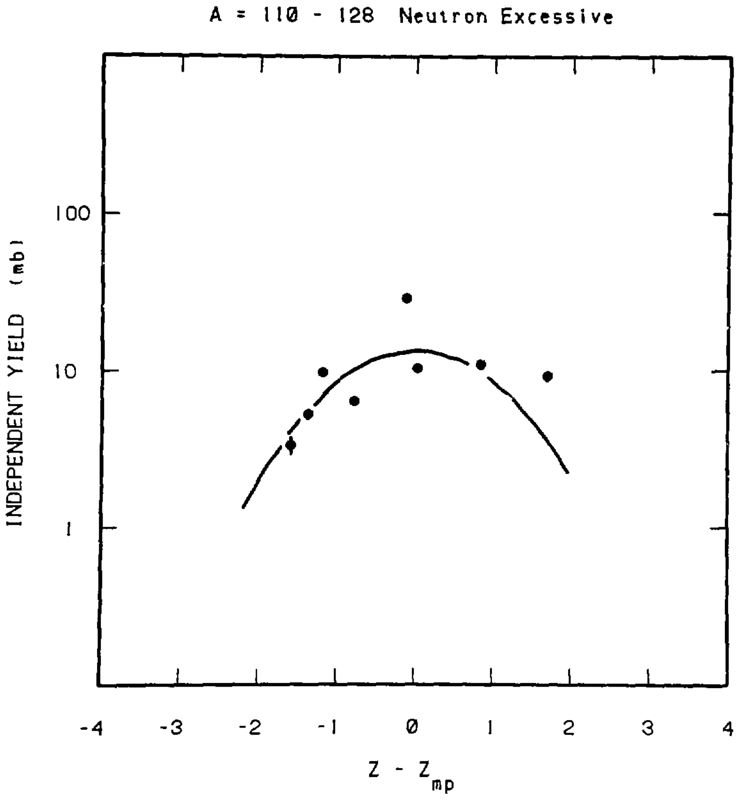
A = 110 - 128 Neutron Excessive
INDEPENDENT YIELD (mb)
100
10
1
-4
-3
-2
-1
0
1
2
3
4
$Z - Z_{mp}$

FIGURE 12.

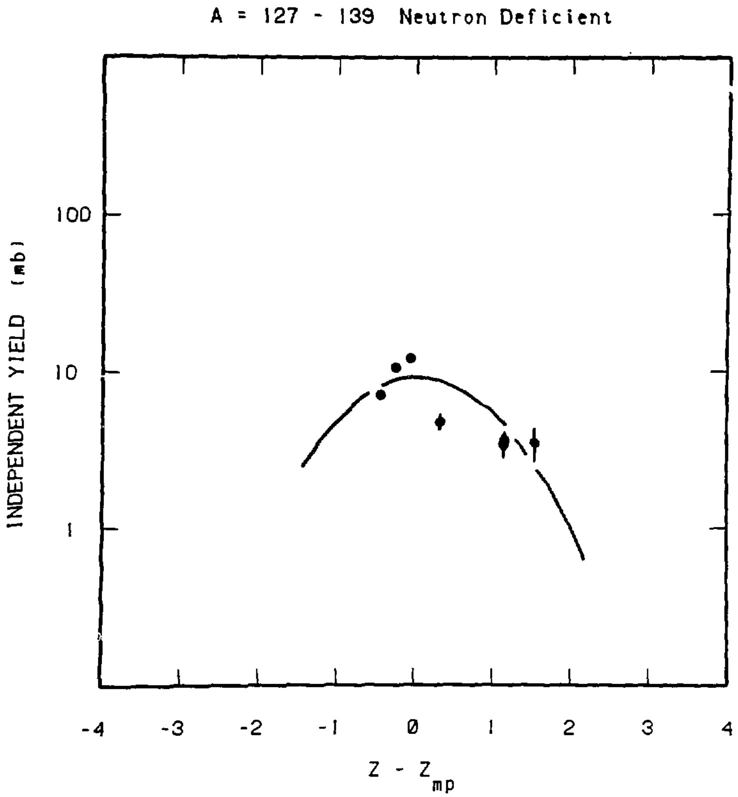
A = 127 - 139 Neutron Deficient
INDEPENDENT YIELD (mb)
100
10
1
-4
-3
-2
-1
0
1
2
3
4
Z - Z
mp

FIGURE 13.

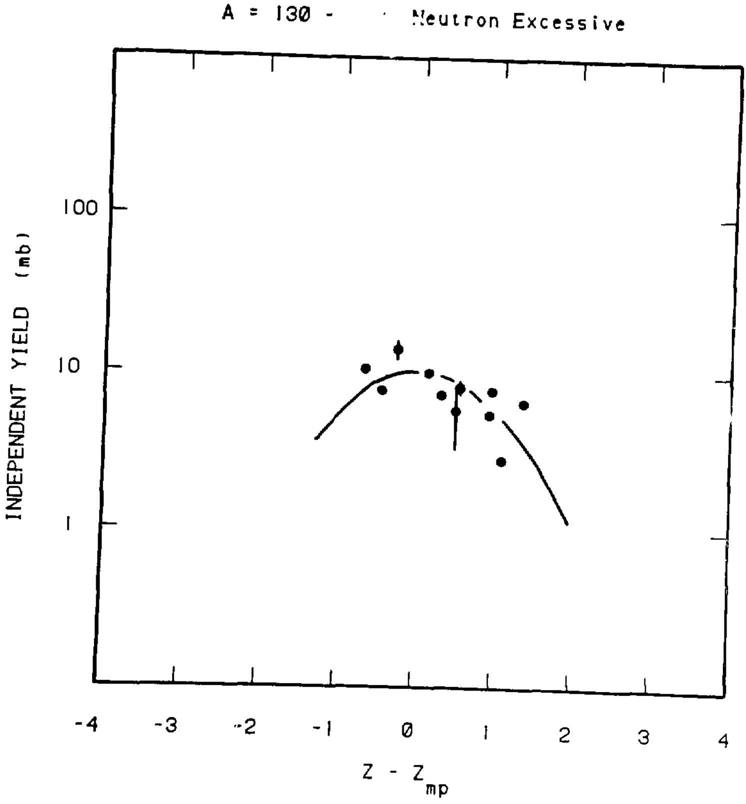
A = 130 - Neutron Excessive
INDEPENDENT YIELD (mb)
100
10
1
-4
-3
-2
-1
0
1
2
3
4
Z - Z_{mp}

FIGURE 14.

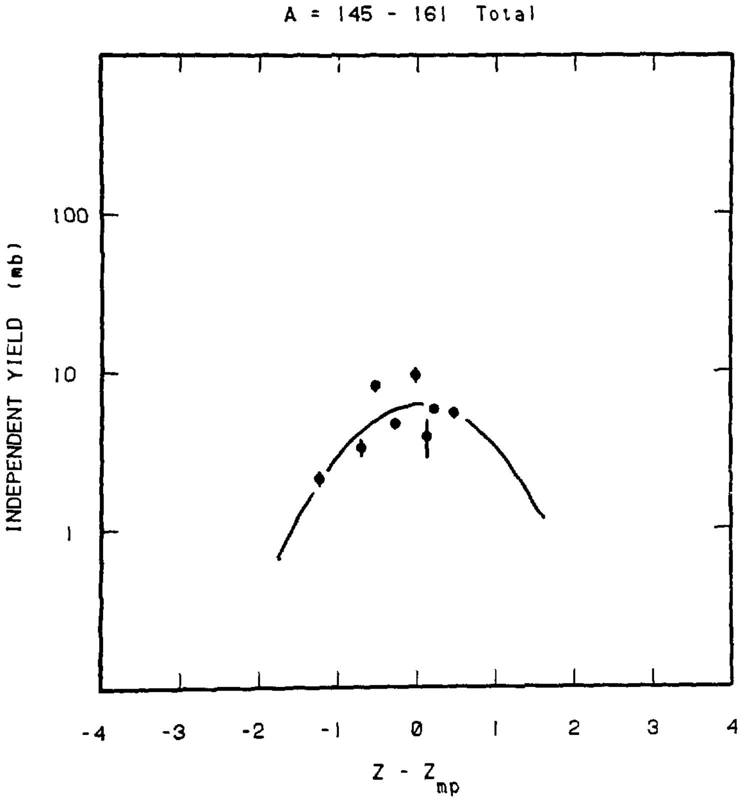

FIGURE 15.

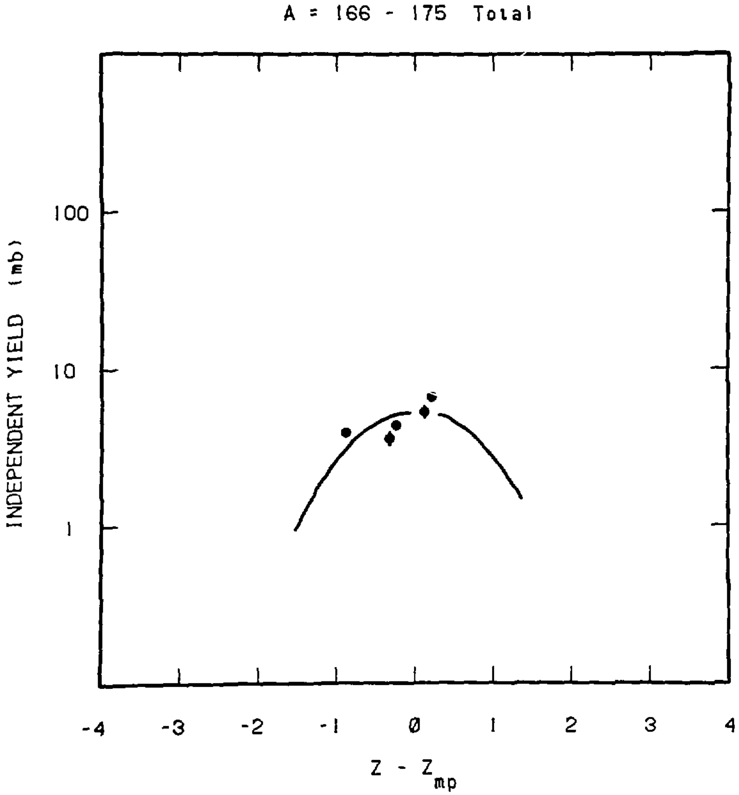

FIGURE 16.

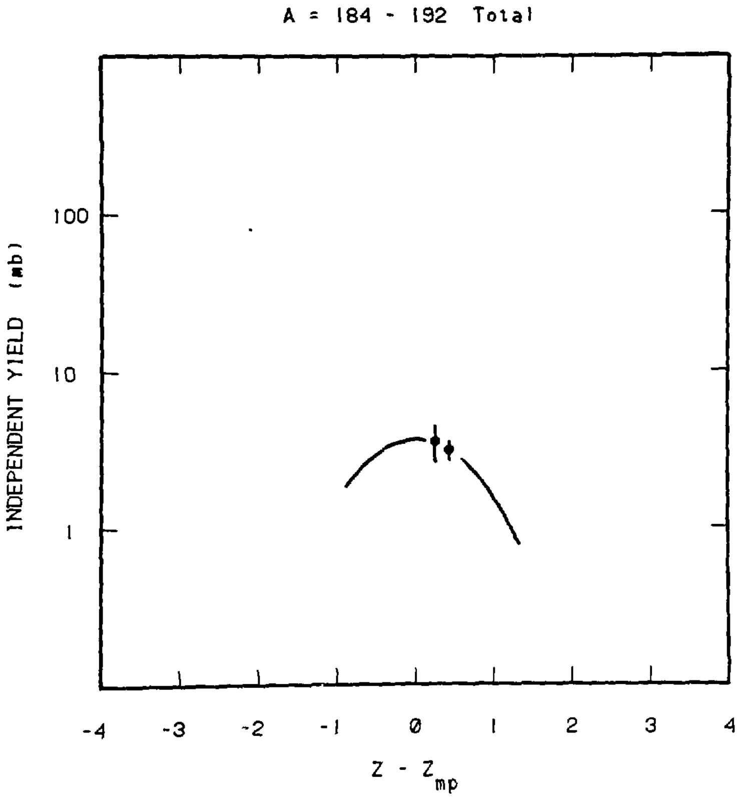

FIGURE 17.

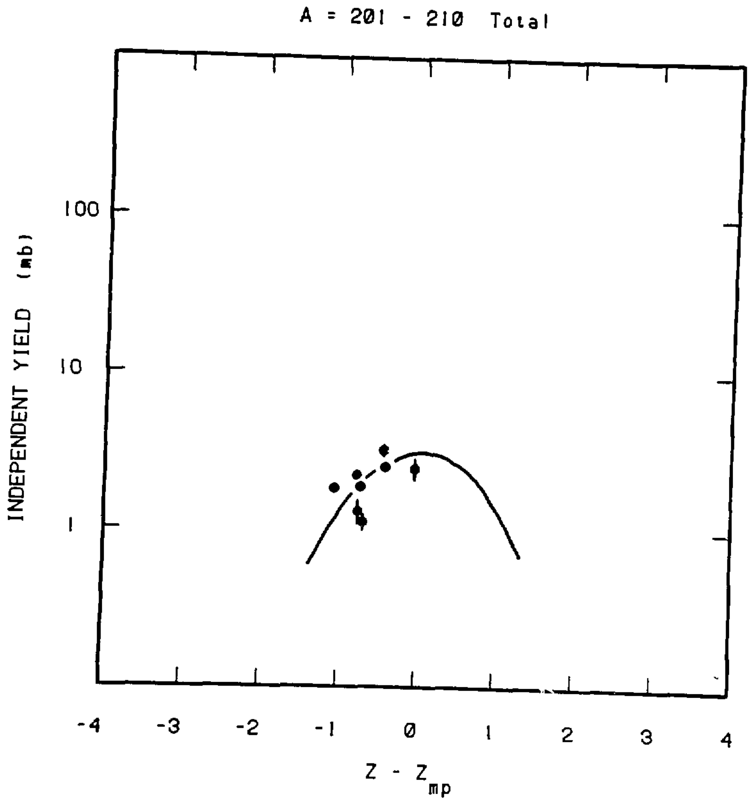

FIGURE 18.

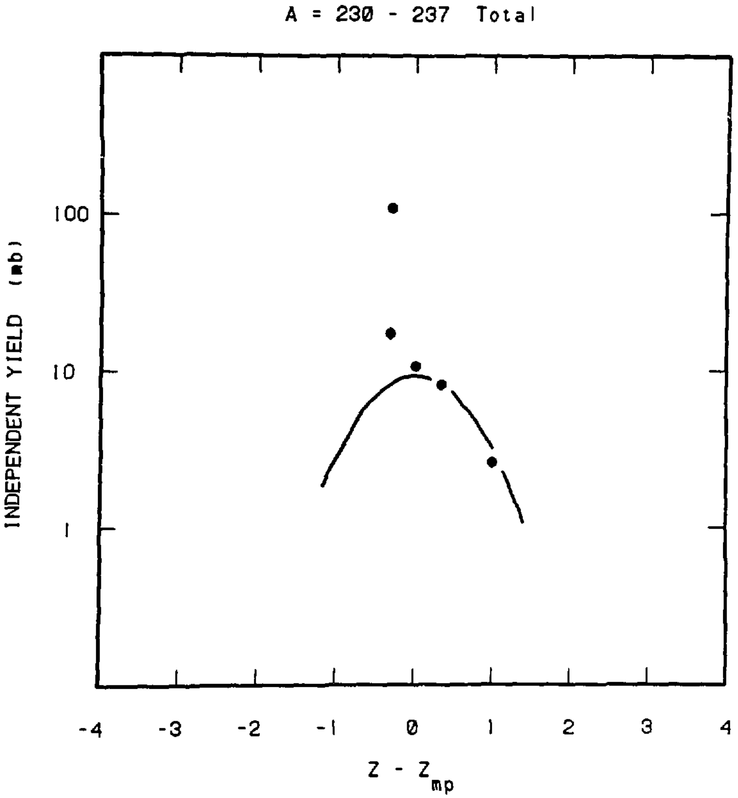

FIGURE 19.

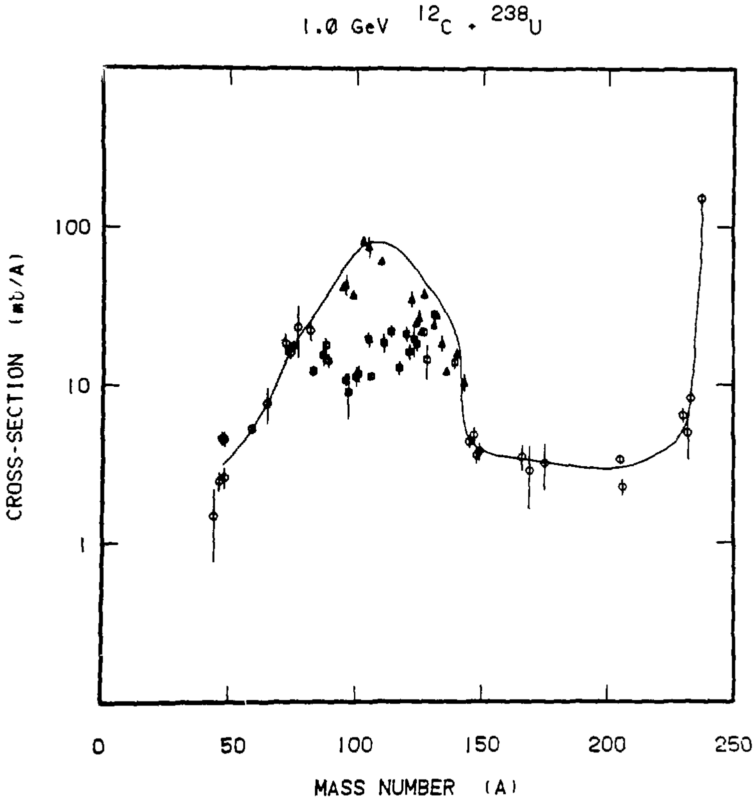
1.0 GeV ^{12}C + ^{238}U
CROSS-SECTION (mb/A)
100
10
1
0
50
100
150
200
250
MASS NUMBER (A)

FIGURE 20.

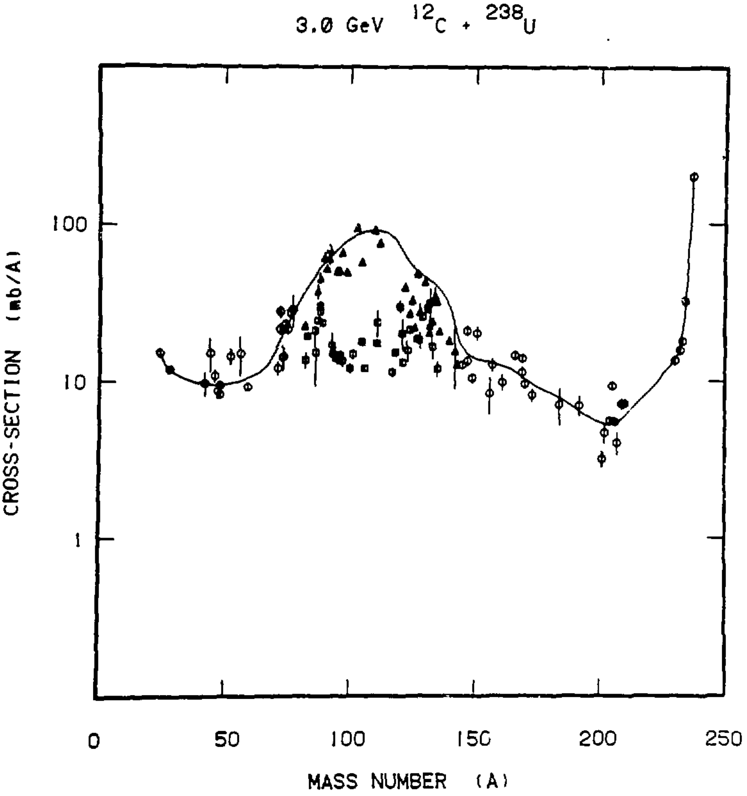
3.0 GeV ^{12}C + ^{238}U
CROSS-SECTION (mb/A)
100
10
1
0
50
100
150
200
250
MASS NUMBER (A)

FIGURE 21.

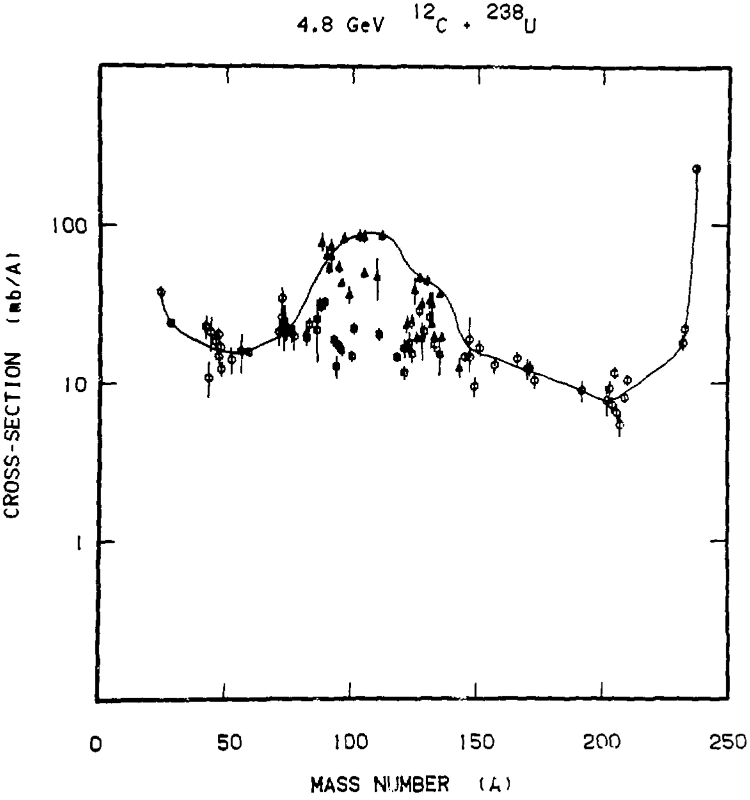
4.8 GeV ^{12}C + ^{238}U
CROSS-SECTION (mb/A)
100
10
1
0
50
100
150
200
250
MASS NUMBER (A)

FIGURE 22.

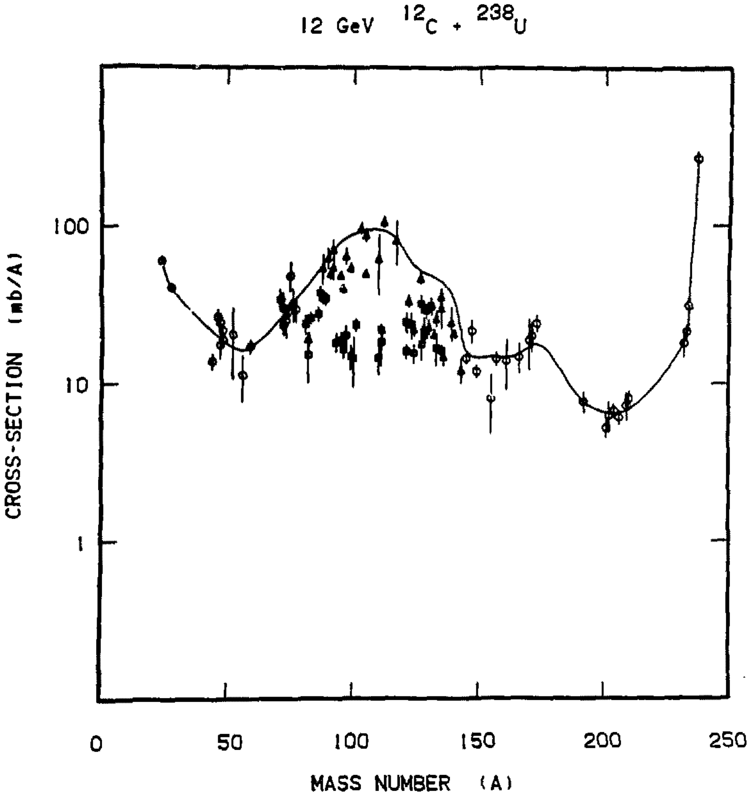
12 GeV $^{12}C + ^{238}U$
CROSS-SECTION (mb/A)
100
10
1
0
50
100
150
200
250
MASS NUMBER (A)

FIGURE 23.

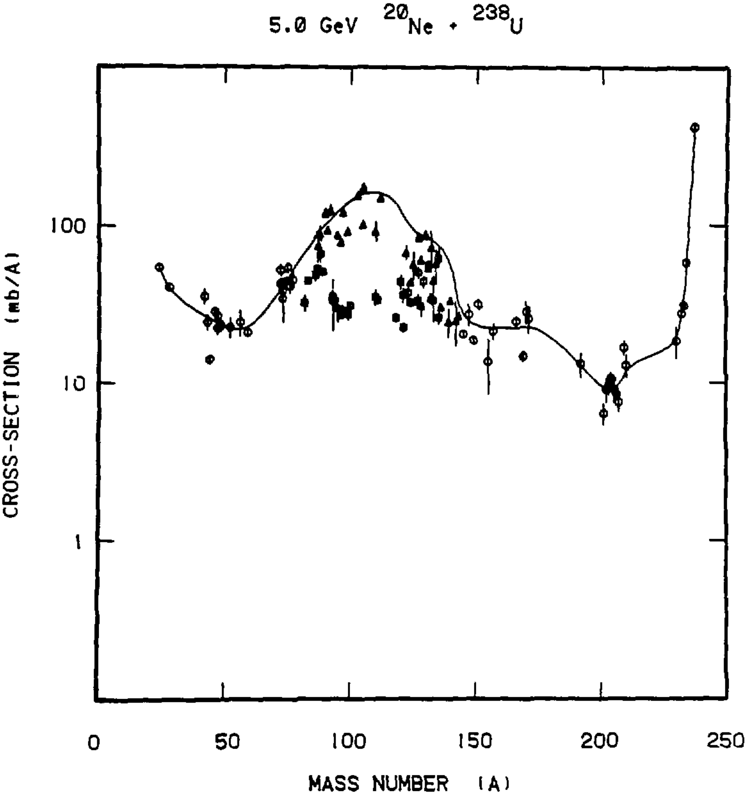
5.0 GeV ^{20}Ne + ^{238}U
100
10
1
CROSS-SECTION (mb/A)
0
50
100
150
200
250
MASS NUMBER (A)

FIGURE 24.

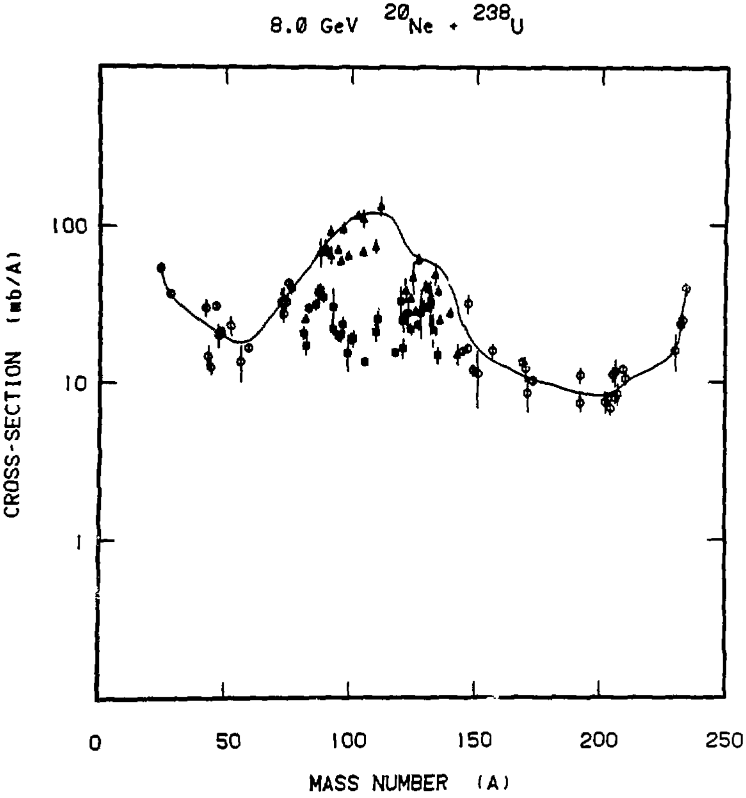
8.0 GeV ^{20}Ne + ^{238}U
CROSS-SECTION (mb/A)
100
10
1
0
50
100
150
200
250
MASS NUMBER (A)

FIGURE 25.

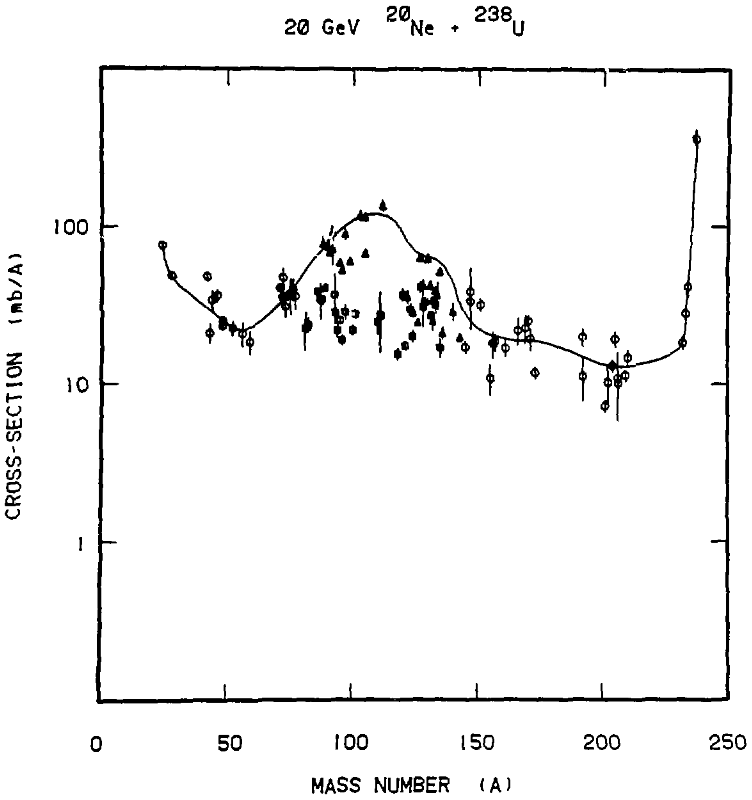
20 GeV ^{20}Ne + ^{238}U
CROSS-SECTION (mb/A)
100
10
1
0
50
100
150
200
250
MASS NUMBER (A)

FIGURE 26.

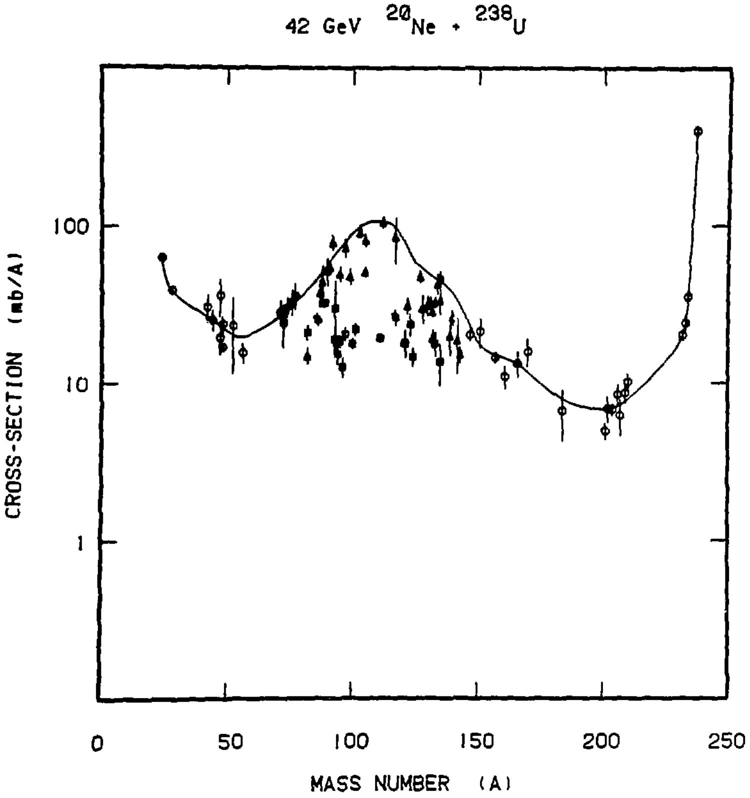
42 GeV ^{20}Ne + ^{238}U
CROSS-SECTION (mb/A)
100
10
1
0
50
100
150
200
250
MASS NUMBER (A)

FIGURE 27.

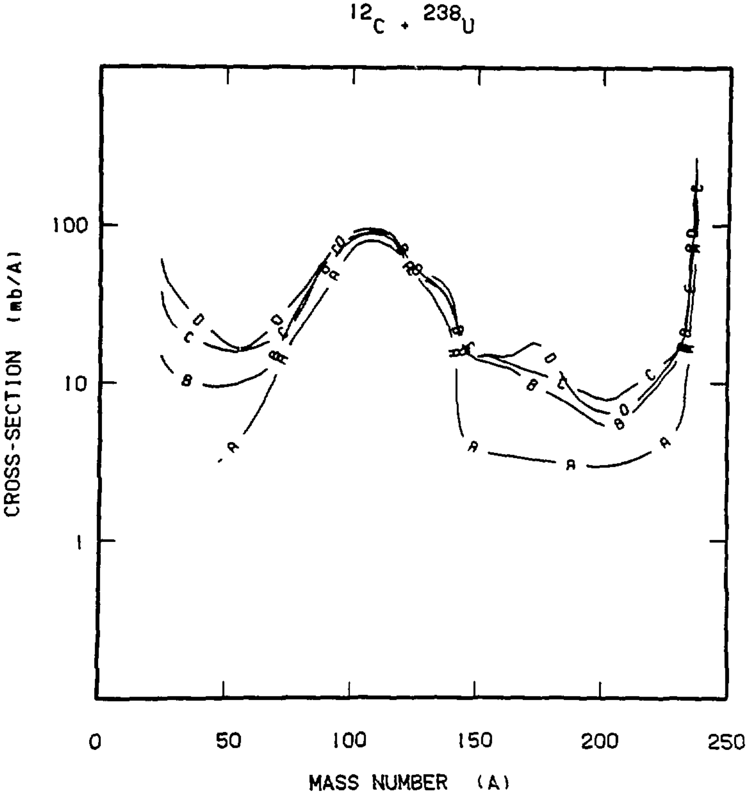
$^{12}C + ^{238}U$
CROSS-SECTION (mb/A)
MASS NUMBER (A)
100
10
1
0
50
100
150
200
250
A
B
C
D

FIGURE 28.

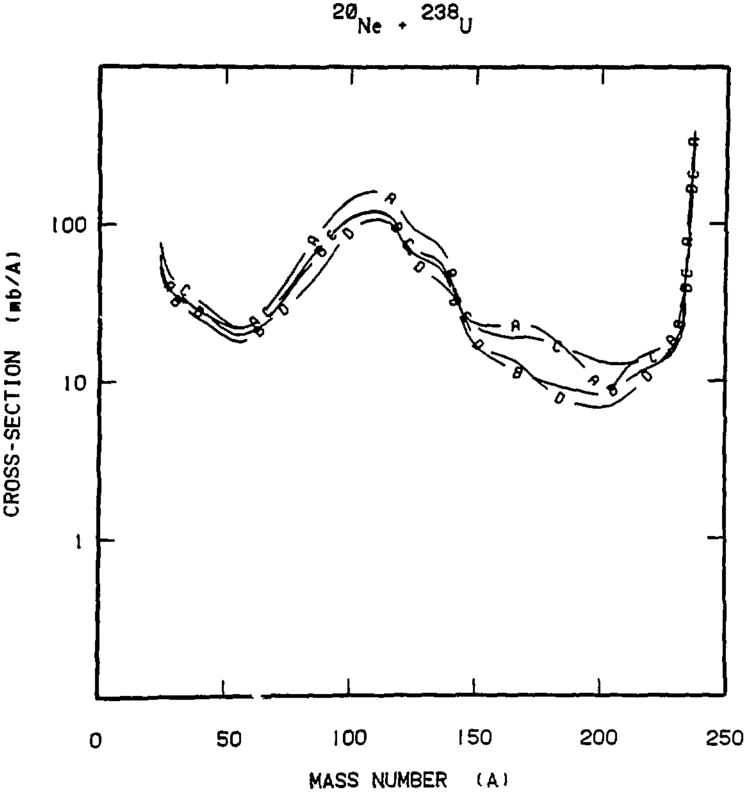
^{20}Ne + ^{238}U
CROSS-SECTION (mb/A)
100
10
1
0
50
100
150
200
250
MASS NUMBER (A)
A
B
C
D

FIGURE 29.

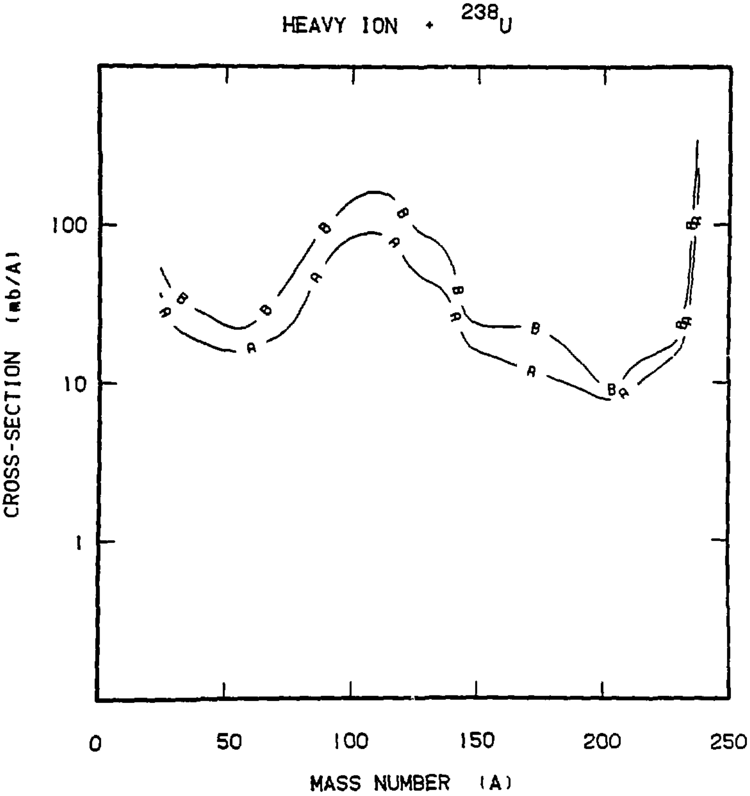
HEAVY ION + ^{238}U
CROSS-SECTION (mb/A)
MASS NUMBER (A)
100
10
1
0
50
100
150
200
250
A
B

FIGURE 30.

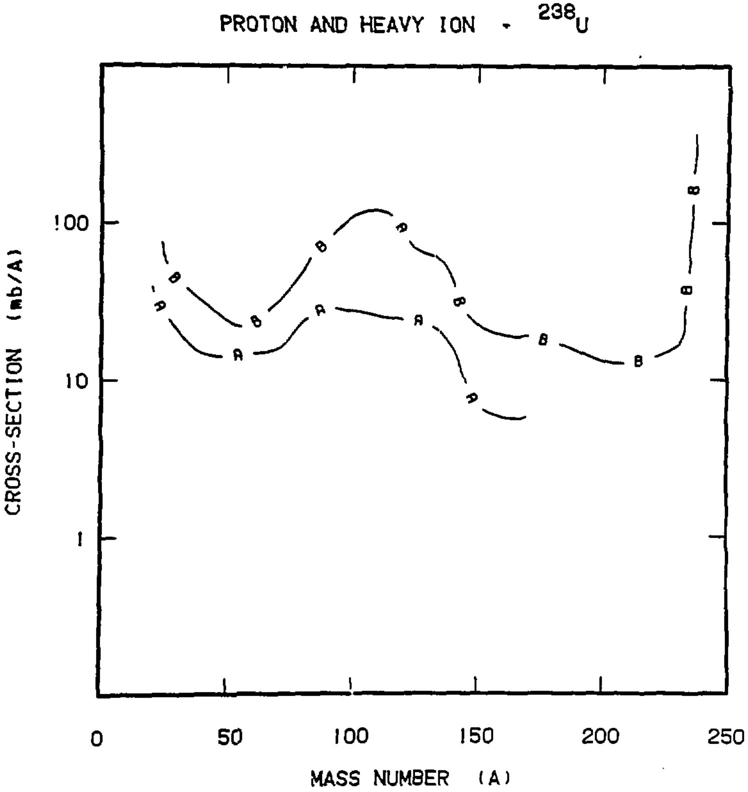
PROTON AND HEAVY ION - ^{238}U
CROSS-SECTION (mb/A)
100
10
1
0
50
100
150
200
250
MASS NUMBER (A)
A
B

FIGURE 31.

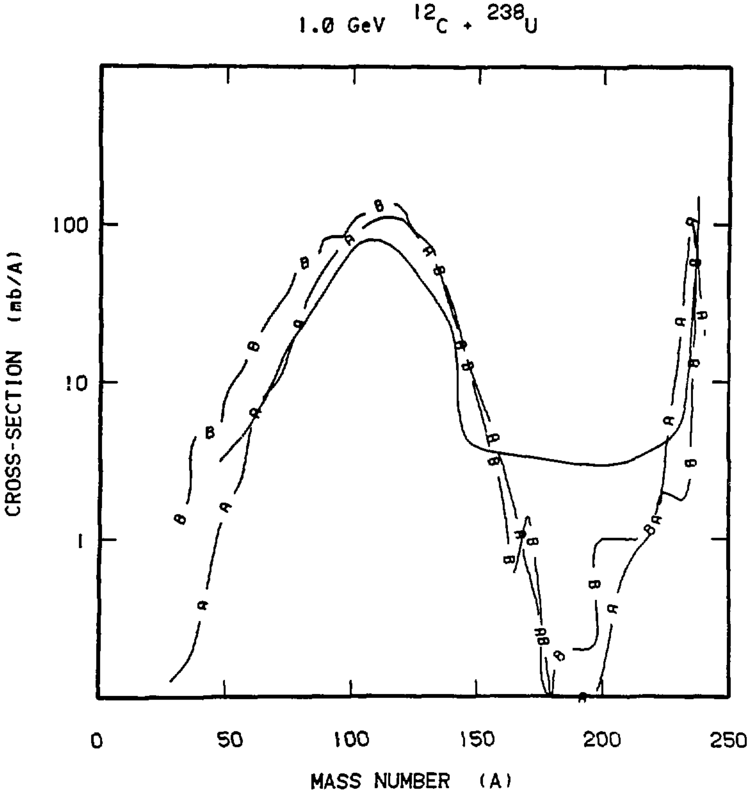
1.0 GeV ^{12}C + ^{238}U
CROSS-SECTION (mb/A)
100
10
1
0
50
100
150
200
250
MASS NUMBER (A)
A
B

FIGURE 32.

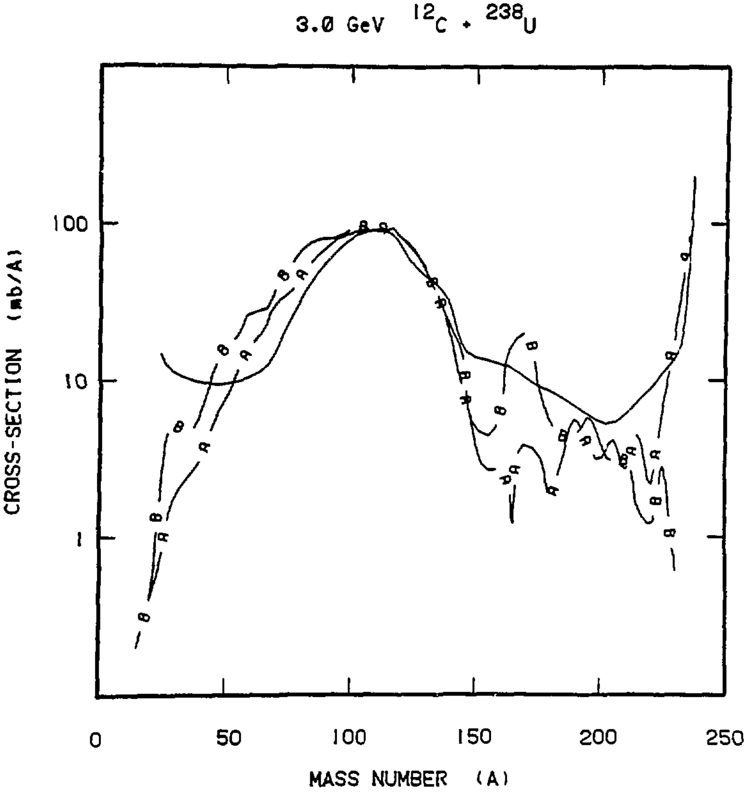
3.0 GeV $^{12}C + ^{238}U$
CROSS-SECTION (mb/A)
100
10
1
0
50
100
150
200
250
MASS NUMBER (A)
A
B

FIGURE 33.

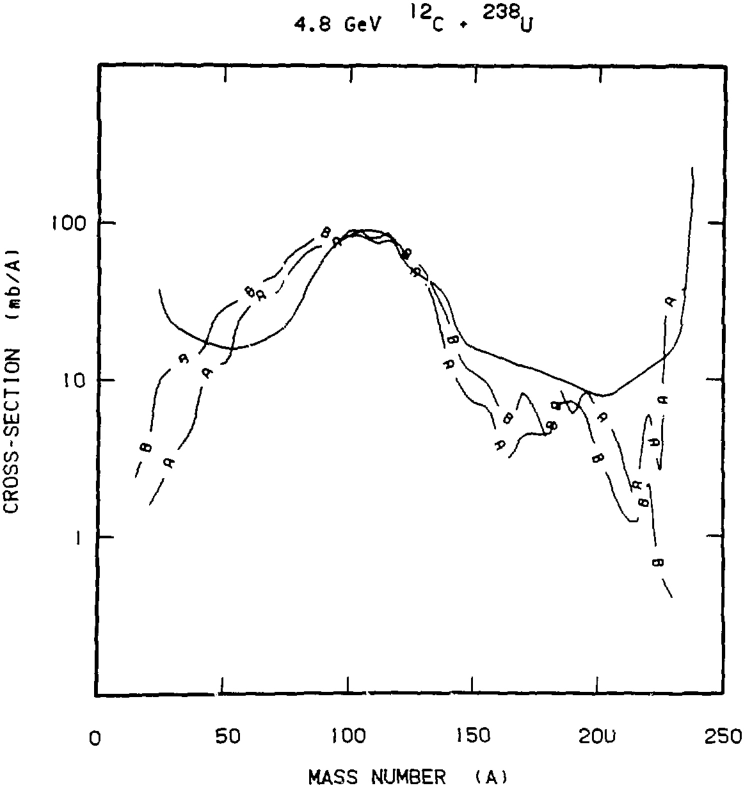
4.8 GeV $^{12}C + ^{238}U$
CROSS-SECTION (mb/A)
100
10
1
0
50
100
150
200
250
MASS NUMBER (A)
A
B

FIGURE 34.

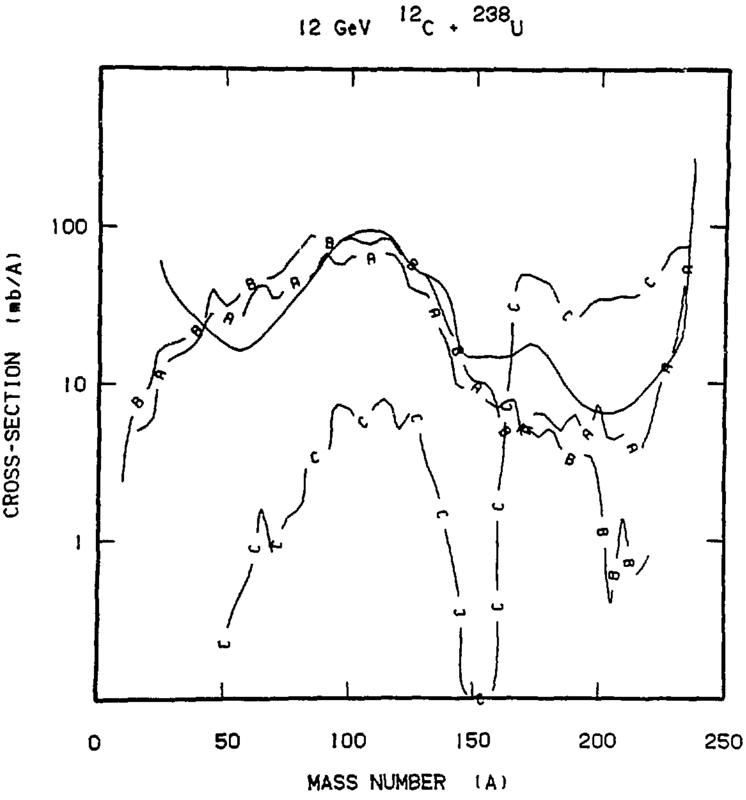
12 GeV ^{12}C + ^{238}U
CROSS-SECTION (mb/A)
100
10
1
0
50
100
150
200
250
MASS NUMBER (A)
A
B
C

FIGURE 35.

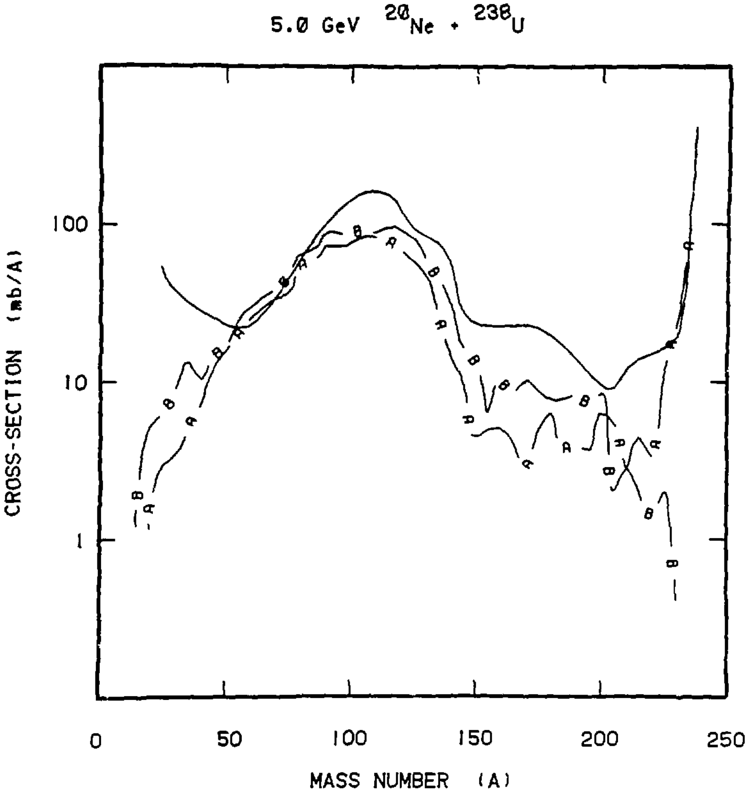
5.0 GeV ^{20}Ne + ^{238}U
CROSS-SECTION (mb/A)
MASS NUMBER (A)
100
10
1
0
50
100
150
200
250
A
B

FIGURE 36.

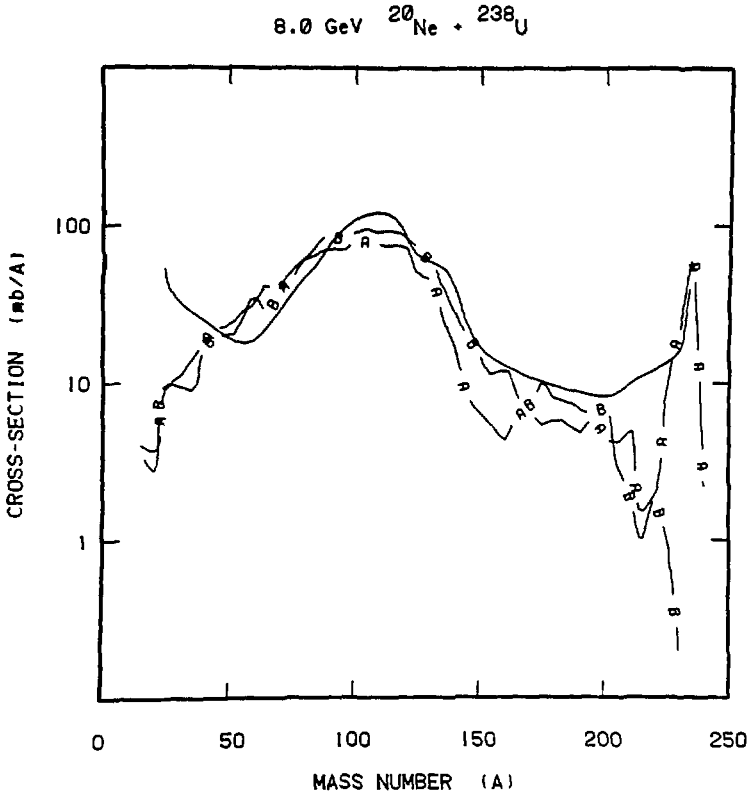
8.0 GeV ^{20}Ne + ^{238}U
CROSS-SECTION (mb/A)
100
10
1
0
50
100
150
200
250
MASS NUMBER (A)
A
B

FIGURE 37.

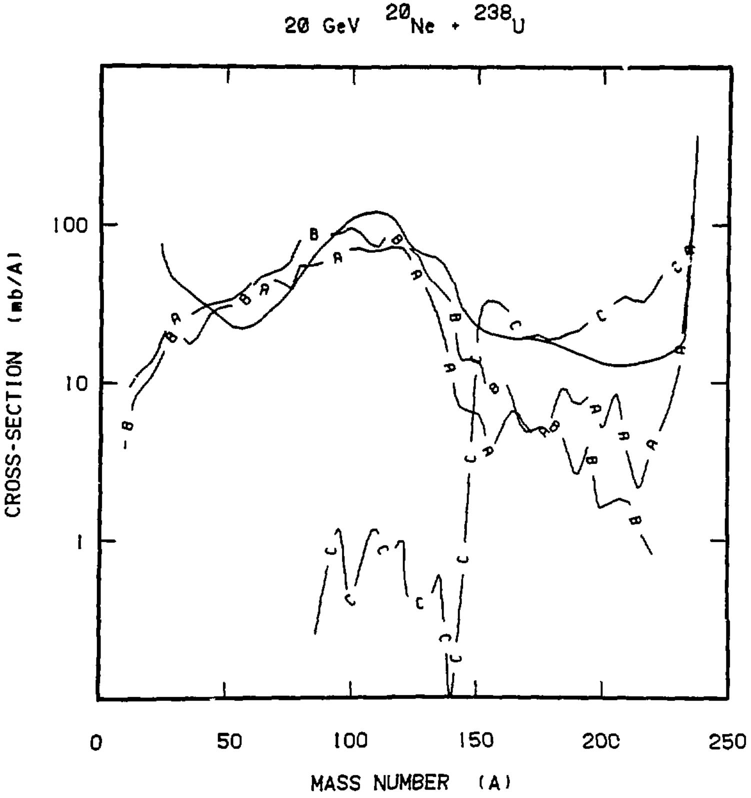
20 GeV ^{20}Ne + ^{238}U
CROSS-SECTION (mb/A)
100
10
1
MASS NUMBER (A)
0
50
100
150
200
250
A
B
C

FIGURE 38.

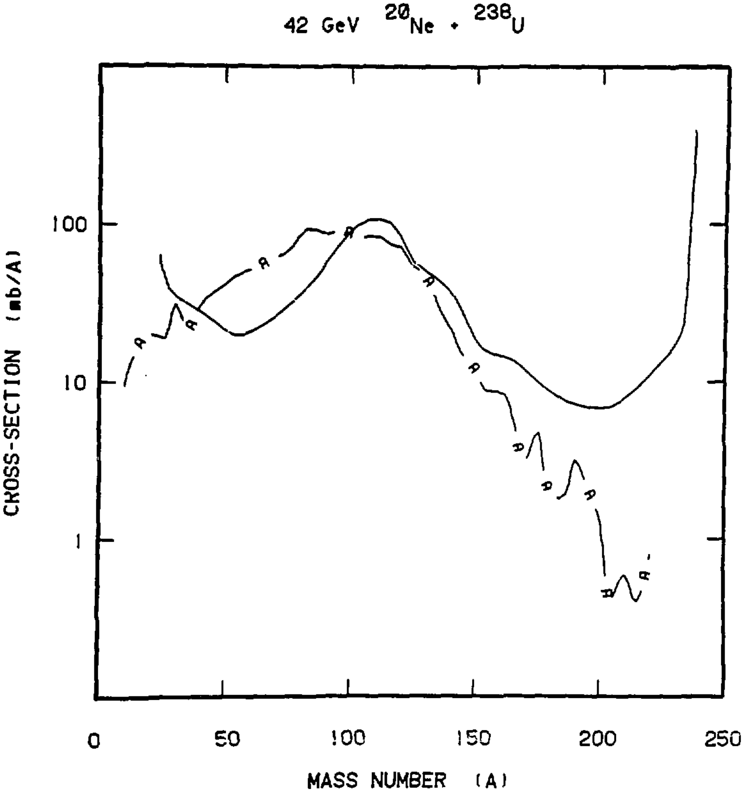
42 GeV ^{20}Ne + ^{238}U
CROSS-SECTION (mb/A)
100
10
1
0
50
100
150
200
250
MASS NUMBER (A)
A

FIGURE 39.

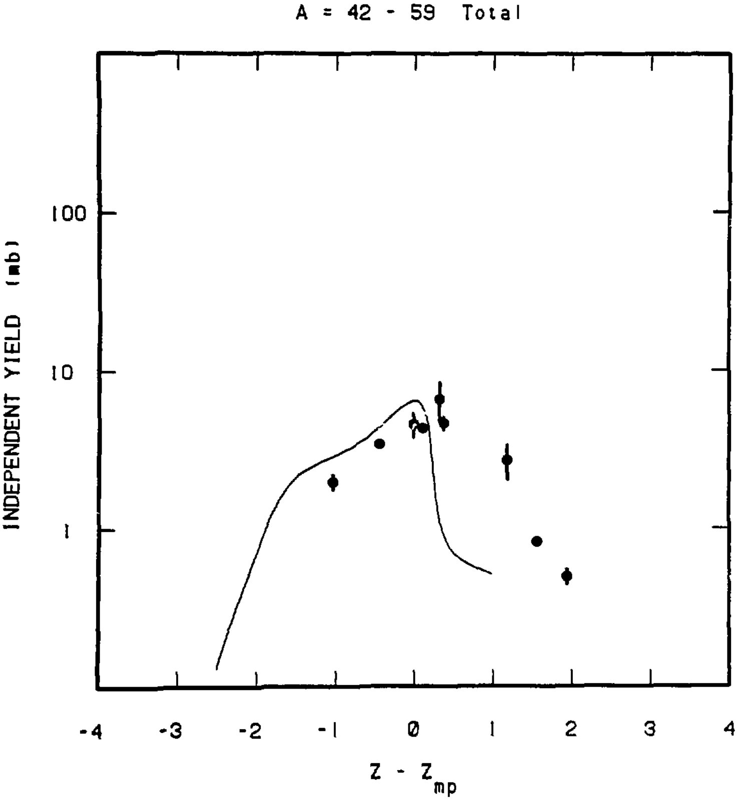

A = 42 - 59 Total

FIGURE 40.

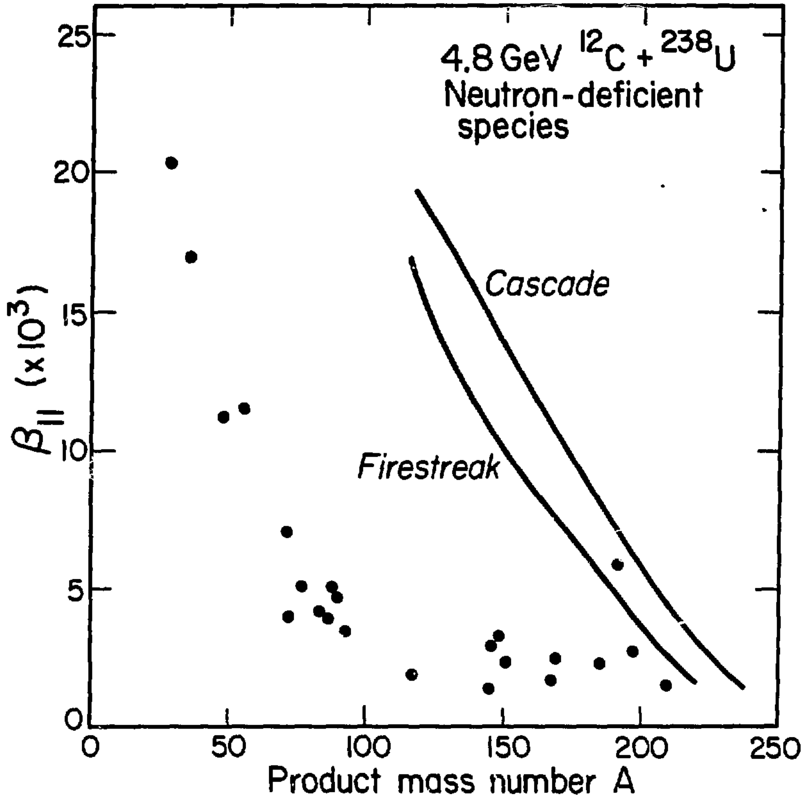

XBL 808-1743

FIGURE 41.